

*A Study of Molecular Gas Associated with  
the HH24 Optical Jets*

*Lifang Ma*

*A thesis submitted in partial fulfillment of the  
requirements for the degree of  
Master of Science*



*Saint Mary's University  
Halifax, Nova Scotia  
August, Nineteen Hundred and Ninety Four*

© Copyright

© 1994 Lifang Ma



National Library  
of Canada

Acquisitions and  
Bibliographic Services Branch

395 Wellington Street  
Ottawa, Ontario  
K1A 0N4

Bibliothèque nationale  
du Canada

Direction des acquisitions et  
des services bibliographiques

395, rue Wellington  
Ottawa (Ontario)  
K1A 0N4

*Your file* *Votre référence*

*Our file* *Notre référence*

**THE AUTHOR HAS GRANTED AN IRREVOCABLE NON-EXCLUSIVE LICENCE ALLOWING THE NATIONAL LIBRARY OF CANADA TO REPRODUCE, LOAN, DISTRIBUTE OR SELL COPIES OF HIS/HER THESIS BY ANY MEANS AND IN ANY FORM OR FORMAT, MAKING THIS THESIS AVAILABLE TO INTERESTED PERSONS.**

**L'AUTEUR A ACCORDE UNE LICENCE IRREVOCABLE ET NON EXCLUSIVE PERMETTANT A LA BIBLIOTHEQUE NATIONALE DU CANADA DE REPRODUIRE, PRETER, DISTRIBUER OU VENDRE DES COPIES DE SA THESE DE QUELQUE MANIERE ET SOUS QUELQUE FORME QUE CE SOIT POUR METTRE DES EXEMPLAIRES DE CETTE THESE A LA DISPOSITION DES PERSONNE INTERESSEES.**

**THE AUTHOR RETAINS OWNERSHIP OF THE COPYRIGHT IN HIS/HER THESIS. NEITHER THE THESIS NOR SUBSTANTIAL EXTRACTS FROM IT MAY BE PRINTED OR OTHERWISE REPRODUCED WITHOUT HIS/HER PERMISSION.**

**L'AUTEUR CONSERVE LA PROPRIETE DU DROIT D'AUTEUR QUI PROTEGE SA THESE. NI LA THESE NI DES EXTRAITS SUBSTANTIELS DE CELLE-CI NE DOIVENT ETRE IMPRIMES OU AUTREMENT REPRODUITS SANS SON AUTORISATION.**

ISBN 0-612-00928-9

**Canada**

## TABLE OF CONTENTS

The Examining Committee	i
Acknowledgments	ii
Abstract	iii
List of Tables	iv
List of Figures	v
<b>I. Introduction</b>	
1. Molecular Outflows and Their Association with Optical Outflows	1
a) Observational properties of outflows	1
b) What drives the molecular outflows ( theoretical models)?	10
2. HH24 Background	15
<b>II. Observations</b>	
	24
<b>III. Results of the Observations</b>	
	29
<b>IV. Physical Conditions of the Gas</b>	
1. Optical Depth	48
2. Excitation Temperature	51
a) Inner Wing	51
b) Outer wing	53
3. Column Density	58
4. Mass, Momentum and Kinetic Energy	59
5. Dynamical age, Momentum Flux and Mechanical Luminosity	63
<b>V. Discussion</b>	
1. General Properties and Morphology of the Outflows	65
2. Relationship to the Optical jets	70

**VI. Conclusion**

72

---

**References**

73

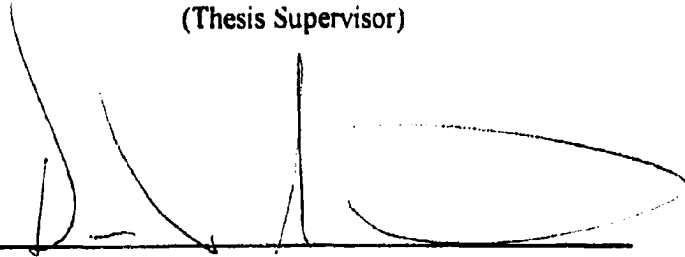
---

**The examining Committee**



---

**Dr. George F. Mitchell  
Department Astronomy & Physics  
Saint Mary's University  
(Thesis Supervisor)**



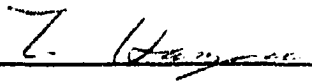
---

**Dr. David B. Guenther  
Department Astronomy & Physics  
Saint Mary's University**



---

**Dr. Malcolm Butler  
Department Astronomy & Physics  
Saint Mary's University**



---

**Dr. Tatsuhiko Hasegawa  
Department Astronomy & Physics  
Saint Mary's University**

## **Acknowledgments**

I would like to thank all people in Department of Astronomy and Physics at Saint Mary's University. Their help and support have made my stay in Halifax really unforgettable and invaluable.

I would like to thank Dr. George Mitchell for suggesting this fascinating thesis topic, for being patient and helpful with my thesis project. I should add a special note of gratitude to him for giving me a unique chance to observe on Mauna Kea, Hawaii. I owe a special debt of gratitude to Dr. David Turner for providing me an opportunity to study in Saint Mary's. I will never forget the warm Christmas Eve I spent with his family. I also wish to thank Dr. Gray Welch for his patience in teaching.

My appreciation, as always, to Dr. Tatsuhiko Hasegawa, for his wise advice, his experience, and his help. I enjoyed many fruitful conversations with him. My special appreciation goes to Dr. David Guenther for all his help and encouragement. It was a very enjoyable experience working with a understanding, insightful and open-minded person like him. I also wish to express my appreciation to Dr. Malcolm Butler for being on my defense committee and for the valuable comments.

I wish to convey my thanks to all my fellow students. To Melvin Blake, who are constantly at my side, introducing me to Eastern Canadians Culture. To Siow Wang Lee, I enjoyed the companionship of her and very glad to have met her. Thanks also to Ken Sills, Wayne Barkhouse, Jean Giannakpoulou, Georgi Mandushev and Yonghui Xie, I wish them the very best in their future.

Most of all, I would like to thank my parents and my sister.  
And, of course, special thanks to my husband.



## ABSTRACT

### A Study of Molecular Gas Associated with the HH24 Optical Jets

*Lifang Ma*

The HH24 complex have been mapped in  $^{12}\text{CO}$  J=3-2 emission at 14" resolution, using the 15m James Clerk Maxwell Telescope ( JCMT ) on Manna Kea, Hawaii. The map in  $^{12}\text{CO}$  J=3-2 shows complicated morphology with at least two outflows emanating from the map center. A blueshifted molecular lobe found in the northeastern part of the map aligns well with the optically detected flow HH24G, while near the map center the  $^{12}\text{CO}$  redshifted flow is coincident with the shocked H<sub>2</sub> region and the optically detected moving gas HH24A. The spatial coincidences of molecular outflows and optical outflows suggest that the two phenomena may physically associated. Analysis of the data shows that the molecular outflow is asymmetric, with the blueshifted flow having 5 times more mass and momentum than the redshifted flow. The momentum flux of the blueshifted outflow which coincides with HH24G is found to be one order of magnitude larger than the momentum of the optical jet. The result implies that the optical jet might be incapable of driving the molecular outflow. However, there are large uncertainty in estimates of momentum flux for both optical jet and molecular outflow .

**LIST OF TABLES**

Table I	Positions and Kinematic Data for HH24	23
Table II	Observational Parameters	26
Table III	Excitation Temperatures at the 6 Selected Positions	57
Table IV	Physical Parameters of Outflows	62
Table V	Characteristics of Outflows	64

## LIST OF FIGURES

Figure 1	Maps of CO Emission from Four Molecular Flows with Differing Spatial Morphology _____	3
Figure 2	Momentum flux vs. Central Source Luminosity and Mechanical Luminosity vs. Central Source Luminosity _____	6
Figure 3	CO J=2-1 Maps of Herbig-Haro Objects in the HH7-11/SVS13 Complex _____	9
Figure 4	Schematic Diagram of the X-Celerator Protostellar Wind Model _____	12
Figure 5	Schematic Structure of a Protostellar Accretion Disk Wind Model _____	14
Figure 6	Large-scale Distribution of the Molecular Clouds in Orion _____	17
Figure 7	The Location of HH24 Complex in Orion B _____	18
Figure 8	An Overview of the [SII] CCD Image in the HH24 Region _____	20
Figure 9	A 254 Spectra $^{12}\text{CO}$ J=3-2 Map _____	27
Figure 10	$^{12}\text{CO}$ J=2-1 and $^{13}\text{CO}$ J=2-1 Spectra at 6 Selected Positions _____	28
Figure 11	Selected $^{12}\text{CO}$ J=3-2, J=2-1 and $^{13}\text{CO}$ J=2-1 Spectra _____	31
Figure 12	Selected $^{12}\text{CO}$ J=3-2, J=2-1 and $^{13}\text{CO}$ J=2-1 Spectra _____	32
Figure 13	The Large Scale CO Contour Map in the HH24-26 Region _____	33
Figure 14	Contour Maps of the Integrated Intensity in Blueshifted and Redshifted Emission _____	34
Figure 15	Channel Maps _____	39
Figure 16	Contour Map of the Redshifted Emission Overlaid on an [SII] CCD Image _____	45
Figure 17	Contour Map of the Blueshifted Emission (from 2 to 5 km s <sup>-1</sup> ) Overlaid on an [SII] CCD Image _____	46
Figure 18	Contour Map of the Blueshifted Emission (from -4 to 8 km s <sup>-1</sup> ) Overlaid on an [SII] CCD Image _____	47

Figure 19	The $^{12}\text{CO}/^{13}\text{CO}$ Intensity Ratio vs. Velocity _____	50
Figure 20	(a): The Theoretical Ratio of $T_{R(32)}/T_{R(21)}$ vs. $T_{\text{ex}}$ and (b): The Ratio $T_{R(32)}/T_{R(21)}$ as a Function of $T_{\text{ex}}$ and Optical Depth $\tau$ _____	54
Figure 21	The Main Beam Temperature Ratio vs. Velocity _____	56
Figure 22	Models of a Conical Bipolar Outflow _____	68
Figure 23	A Schematic Diagram of the Paraboloidal Outflow Model _____	69

## I. Introduction

### 1. Molecular outflows and their association with optical outflows

It is now accepted generally that young stellar objects ( YSOs ) of all masses undergo a phase of mass loss during their evolution to the main sequence. Evidence for such mass outflows is provided by a variety of observed phenomena. Two of the most striking of them are highly collimated, fast, optically detected outflows ( also known as Herbig-Haro jets and Herbig-Haro objects ) and less well collimated, slower, molecular outflows detected at mm/submm wavelengths. It has long been believed that the two types of flows must be related. There is, however, no agreement on whether they are different manifestations of winds emerging from the central source or whether the small-scale jets are powering the large-scale molecular outflows. The argument has been concentrated mostly on whether or not the optical jet has enough momentum to drive the molecular outflows. Moreover, although a spatial overlap of molecular outflows and HH objects is already striking, only a limited number of molecular outflows have been found around HH jets because of various observational selection effects. In this thesis we present  $^{12}\text{CO}$  J=2-1, J=3-2 and  $^{13}\text{CO}$  J=2-1 molecular observations towards the HH24 complex. The primary goal of this study is to carry out a search for the connecting evidence between these two types of flows. Some salient observational features of molecular outflows, their relationship to optical outflows, and the driving mechanism for the molecular outflows are summarized below.

#### a). Observational properties of outflows

Since the detection of broad line wings of  $^{12}\text{CO}$  in the core of the Orion A molecular cloud ( Zuckerman et al. 1976, Kwan et al. 1976 ), it has been realized that the high velocities of  $^{12}\text{CO}$  are a result of outflow motions caused by the energy release from deeply embedded objects. This realization is based on the fundamental observational properties of the molecular flows. The bipolar structure, the high velocities, the large spatial extent, and the large mass cannot be explained by collapse, rotation or turbulent motion ( Bally & Lada 1983 ). In fact, it has been suggested that a star cannot form without outflow because they may provide the only means for a collapsing and rotating object to shed sufficient angular momentum to grow to stellar dimensions ( Shu et al. 1987 ). So far nearly 200 molecular outflows have been found by their broad mm-wavelength  $^{12}\text{CO}$  emission lines ( Bally and Lane 1991 ). Many of the outflows share a number of common characteristics, which provide important clues to, and constraints on, the mechanisms which drive the outflows. The most remarkable feature of the molecular outflows is their tendency to be bipolar, with redshifted gas ( red lobe ) located on one side of the source and blueshifted gas ( blue lobe ) located on the other ( Fig. 1 ). It has been suggested that most material in the lobe is confined to a relatively thin, swept-up shell since the observations show a degree of limb-brightening ( Snell et al. 1984, Moriarity-Schieven & Snell 1988, Moriarity-Schieven et al. 1989 ). However, the observational data show considerable variety for different sources. It is accepted generally that the lobes contain regions of low density, but they are not completely empty in general. The degree of collimation of the lobes ( length : width ratio ) varies from about 1 ( poorly collimated)

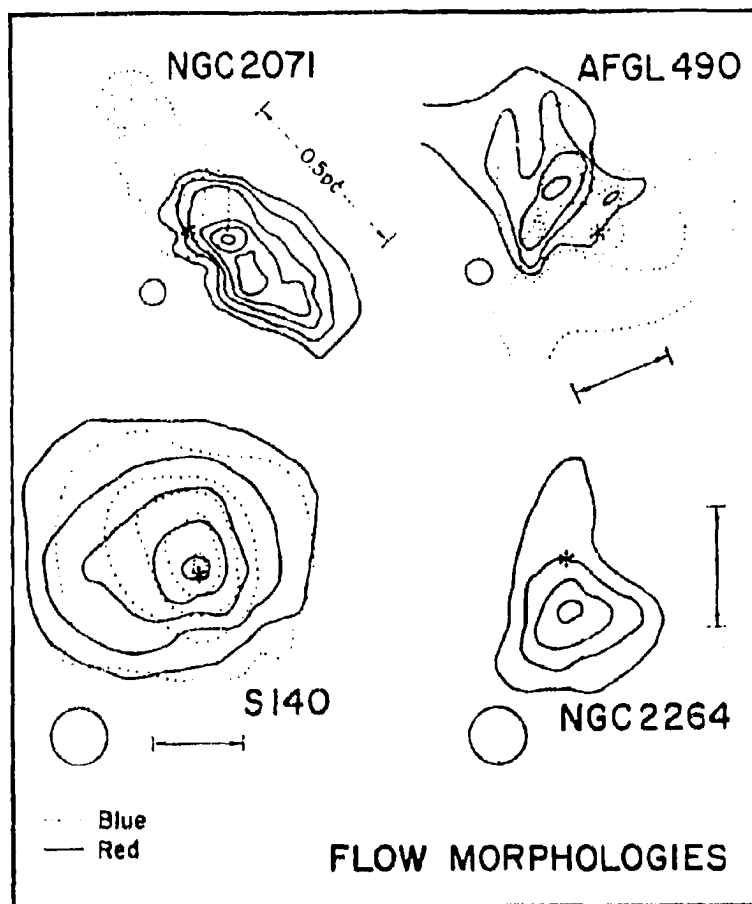


Figure 1. Maps of  $^{12}\text{CO}$  emission from four molecular flows with differing spatial morphology taken from Lada ( 1985 ). NGC2071 is a highly collimated bipolar flow while AFGL490 is a poorly collimated bipolar flow. S140 is an example of a isotropic flow while NGC2264 is a monopolar source in which only redshifted molecular emission is observed.

to over 10 ( highly collimated ). A statistical study shows that the majority of bipolar flows have a moderate degree of collimation ( Fukui et al. 1991 ).

Typical molecular outflow masses range from  $0.1 \sim 170 M_{\odot}$  ( Fukui et al. 1991 ). As can be seen, many outflows have a large excess of outflow mass over stellar mass. The large mass of molecular outflow and the fact that the velocity field of the molecular outflow is clearly distinct from that of the ambient cloud indicate the molecular flows are primarily made up of swept up ambient materials. The large mass also indicates that outflows are a very energetic phenomenon. Typical molecular outflow momenta and kinetic energies range from  $0.1 \sim 1000 M_{\odot} \text{ km s}^{-1}$  and  $10^{43} \sim 10^{47} \text{ erg}$ , respectively. Therefore, molecular outflow phenomena must have an important effect on their surrounding circumstellar material and on the future development of star formation in clouds that they occupy.

The fact that molecular outflows are more frequently associated with highly embedded infrared sources than with optically visible YSOs suggest that the outflow phase occurs very early in the life of a young star and may coincide with the main accretion phase of the protostellar objects. The dynamical age ( defined as  $t_{\text{dyn}}$  ) of a molecular outflow is obtained by dividing the outflow physical size ( typically  $0.04 - 4 \text{ pc}$  ) by the characteristic velocity ( typically  $3 - 150 \text{ km s}^{-1}$  ). Recent studies by Margulis and Snell ( 1989 ), Koo ( 1990 ), Bachiller et al. ( 1991 ), and Mitchell and Hasegawa ( 1991 ) have found several extremely high velocity outflows with the linewidths ranging from 100

$\text{km s}^{-1}$  to over  $300 \text{ km s}^{-1}$ . Depending on the choice of the velocity, the typical dynamical ages of molecular outflows are found to be in the range of  $1 \times 10^3 \sim 2 \times 10^5$  years. On the assumption that the apparent dynamical time scale represents the true age of the flow, the dynamical ages have been used in analyses of momentum injection rate ( $=MV/t_{\text{dyn}}$ , where  $M$  is the outflow mass,  $V$  is the outflow characteristic velocity) and the mechanical luminosity ( $=MV^2/2t_{\text{dyn}}$ ). Bally and Lada (1983), Lada (1985) and Mozurkewich et al. (1986) found that, on average, the momentum flux is two or three orders of magnitude greater than what can be provided by radiation pressure ( $=L_*/c$ , where  $L_*$  is the radiation luminosity of the central source). At the same time, the mechanical luminosity is typically several orders of magnitude less than the radiative luminosity. These properties imply that the outflows can not be accelerated by the radiation pressure alone. On the other hand, only a small fraction of the radiated power needs to be converted into mechanical energy. The momentum flux and mechanical luminosity as a function of bolometric luminosity of the source are shown in Figure 2. The recent statistical study by Parker et al. (1991) suggests that the outflow duration is an order of magnitude greater than commonly assumed, and comparable to the lifetime of the YSOs ( $\sim 2 \times 10^5 \text{ yr}$ ). Such large ages may provide a way to alleviate the momentum supply problem.

The optical outflows are traced by HH jets and HH objects. HH objects come in several forms. A particularly interesting subset is formed by the highly collimated HH jets strongly interacting with the ambient gas. This class of HH objects often resemble bow

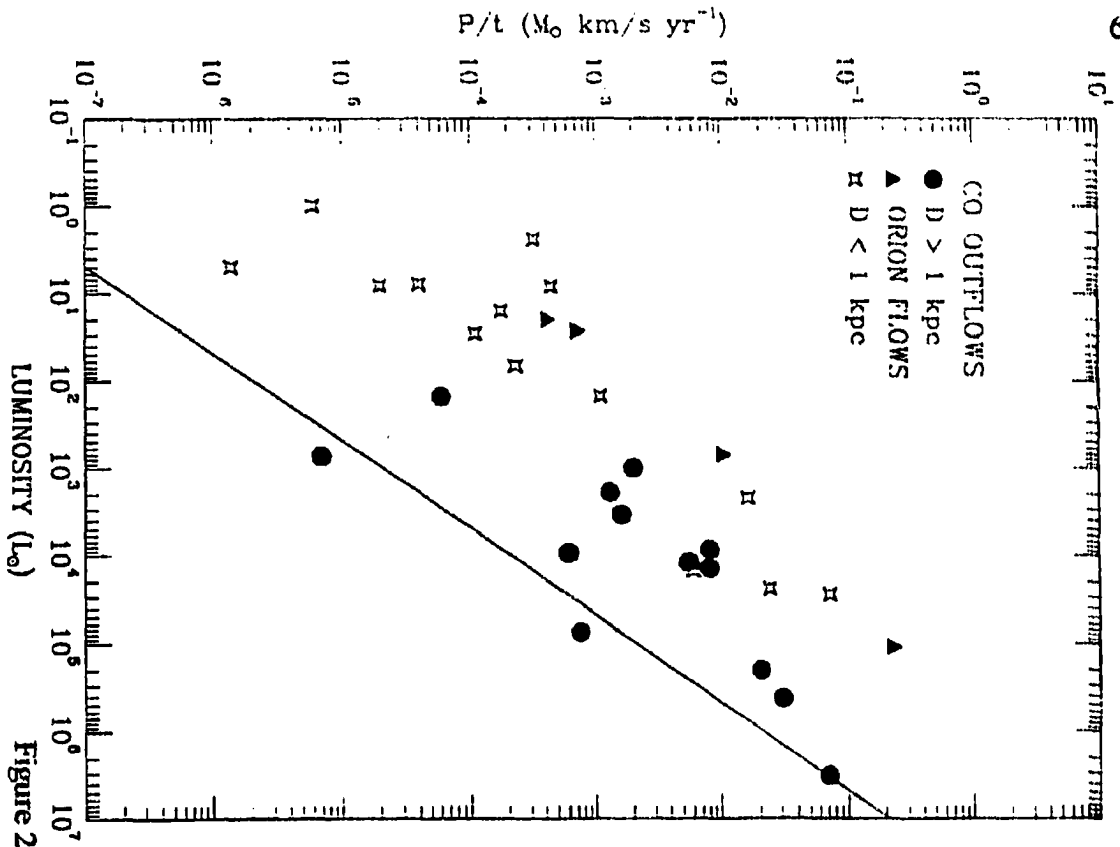
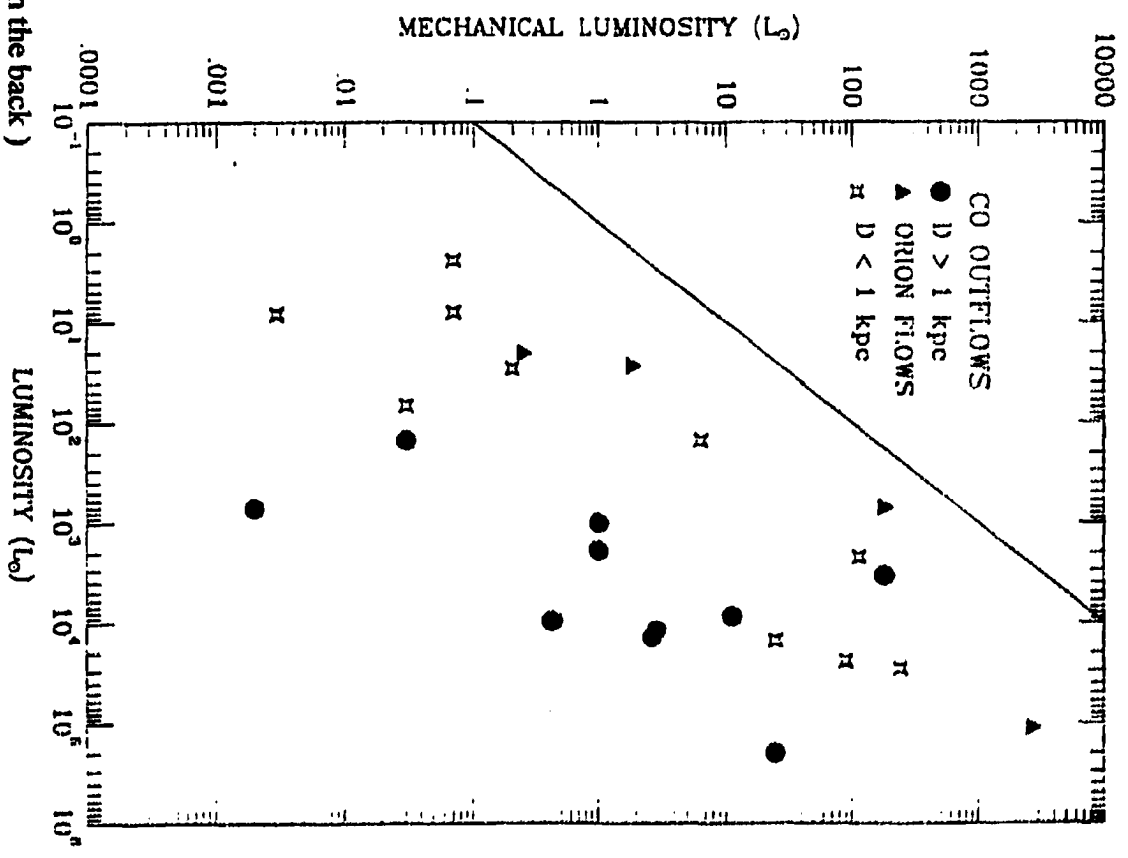


Figure 2. (Caption is on the back)



shocks where ambient material is accelerated in the direction of the jet while at an inner shock the jet material is decelerated. A HH jet is defined as an elongated, highly collimated, knotty structure with an HH-like spectrum ( Mundt 1988 ). Since the discovery of the first HH jets ( Dopita et al. 1982, Mundt et al. 1983, 1984 ), 30 jets have been reported in literature ( Mundt, 1993 ). A common feature of all known jets are their knotty structure with bow shock-like HH objects or bright knots marking the end of a jet. Usually the bow shock HH objects display higher excitation lines than those of the HH jets. The knots provide a means to measure the proper motion of jets. Studies show that typical proper motions are in the range 200 to 300 km s<sup>-1</sup>, which is comparable with the radial velocity ( 100 ~200 km s<sup>-1</sup> ). The proper motion vectors directed away from the source provide the evidence that they are a manifestation of mass outflow phenomena.

Approximately 50 % of the flows traced by HH objects and jets are bipolar ( Edward et al. 1991 ). Of the remainder, normally only the blueshifted component is seen. This is probably due to the redshifted component being buried systematically deeper in molecular clouds, hidden from view by large extinction. The opening angles of the jets are in general small, ranging from 5° to 20°. The opening angle of some of the most highly collimated flows ( e.g. HH 30 jet ) are as small as 1°.

HH objects and jets are found to be associated with both embedded sources and optically visible pre-main-sequence stars. Edward et al. ( 1991 ) suggested these may indicate that the sources which show both optical and molecular outflow phenomena may

be the transition objects between the embedded and optically visible phases. Typical length for the optical outflows is 0.01 -1.00 pc and a typical dynamical time is about  $10^3$  yr. The dynamical time of optical outflows is found to be smaller by at least one order of magnitude than the corresponding value for molecular outflows. If the dynamical time of the molecular outflow represents the total time that the source has been in the outflow phase then this suggests that optical outflow may be an intermittent phenomenon ( Edwards et al. 1991 ). Indeed, intermittence is indicated by several observations ( Reipurth 1989, Hartigan et al. 1990, Mitchell et al 1991 ).

Despite the incompleteness of searches and various selection effects, it is already clear that the molecular and optical outflows are associated phenomena. The direct evidence that indicates the connection between the two types of flows is their similar overall flow directions. Good examples include L1551/IRS5 ( Snell et al. 1985, Moriarity-Schieven & Snell 1988, Fridlund et al. 1989 ), the HH 7-11/SVS13 complex ( Snell & Edwards 1981, Bachilter & Cernicharo 1991 ) ( Fig 3 ), and the HH46/47 jet complex ( Chernin & Masson 1991 ). In most cases, the HH objects or jets are located along the axis of the blue lobe of molecular outflows which usually offers less extinction than the red lobe.

Besides the preliminary evidence mentioned above, the energetics of the two types of outflows are seen to scale with the bolometric luminosity of the source in the same way. Levreault ( 1988 ) has shown that the mass loss rate in the wind driving a molecular outflow scale with the source bolometric luminosity roughly as  $L_{bol}^{0.6}$ . The same scaling

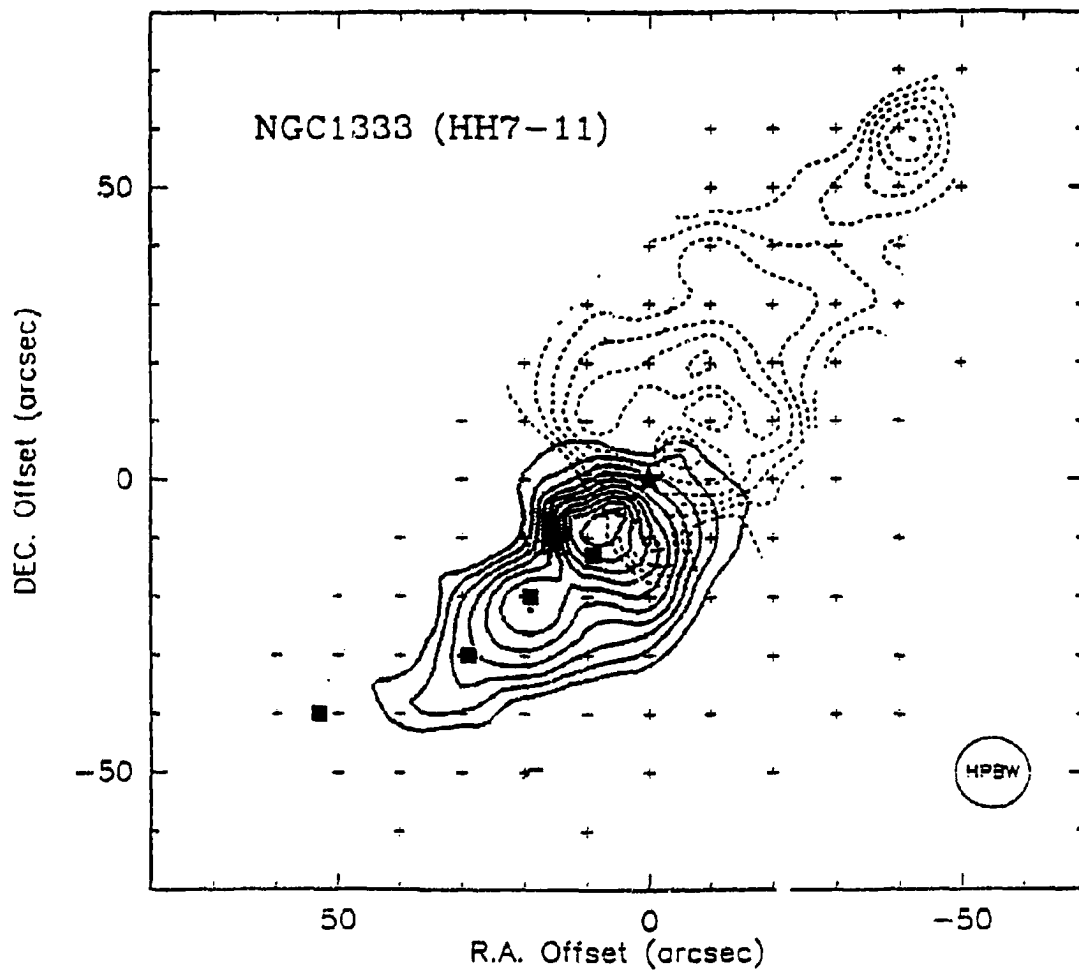


Figure 3.  $^{12}\text{CO}$  J=2-1 maps in the HH7-11/SVS13 complex ( Taken from Bachiller and Cernicharo 1991 ). The blueshifted lobe ( solid ) is closely associated with the Herbig-Haro objects HH7-11 mostly along the axis of the molecular outflow.

law with source luminosity is found for the mass loss rate from jet ( Ray et al. 1991 ). Since the mass loss rates of both jets and molecular flows driving winds scale roughly with the same power of  $L_{\text{bol}}$ , it is likely that the jet is at least a component of the initial wind from the driving source. However, as pointed out by Mundt et al. ( 1987 ) and Ray et al. ( 1990 ), the mass loss rates and the momentum flux in the jets are one to two orders of magnitude too small to be responsible for molecular outflows. The discrepancies in mass loss rate and in momentum flux between the jet and the molecular flow have led to suggestions that the jet can be as perhaps only the central component of a largely unseen neutral wind. Such neutral wind have been observed in the bipolar flow source HH7-11 by Lizano et al. ( 1988 ). However, based on an analysis of recent jet models, Raga ( 1991 ) found the mass loss and the momentum flux to be, on average, 300 times larger than those given by Mundt et al. ( 1987 ). Moreover, the revised molecular flow ages ( greater than  $10^5$  yr. Parker et al. 1991 ) can also help to remove the discrepancy ( Padman & Richer 1993, Masson & Chernin 1993 ).

b). What drives the molecular outflows ( theoretical models )?

It is now generally believed that the bipolar molecular lobes consist mostly of ambient gas that has been swept up by a much higher velocity wind emanating from the central region. Ordinary stellar winds driven by radiation pressure have been shown to be inadequate to account for the large momentum flux that is needed to drive a molecular outflow ( see I.1(a) ). In addition, such an initially isotropic stellar wind requires that the

ambient cloud have an anisotropic density-gradient which is conducive to form "interstellar nozzles", in order to explain the outflow collimation. However such a nozzle appears to have serious stability problems ( Blandford & Rees 1974, Dyson 1987 ). Therefore, magnetohydrodynamic wind models that employ the gravitational energy of accreted material or the rotational kinetic energy of the star are commonly favored. The main debate concerns whether the winds originates from the star, from the disk or from the boundary between them.

The physics of a centrifugally driven wind from a rapidly rotating magnetic protostar has been analyzed in a variety of contexts by Draine ( 1983 ), by Hartmann and MacGregor ( 1982 ), and by Shu and his collaborators ( 1988 ). The latter group of authors proposed a centrifugal wind model to explain the different behaviors of the optical jets ( called ' ordinary wind' by these authors ) and the extraordinary wind. In this model, the extraordinary wind is produced by the " X - celerator mechanism " ( Fig.4 ). The wind begins in a band in the high-density photospheric regions at the protostellar equator. The gas pushed out from the x-point ( where the centrifugal force balances gravity ) by the thermal pressure. The ejected gas is coupled to the outside magnetic field which corotates at the protostellar angular velocity  $\Omega_*$ . The gas is centrifugally accelerated out to the Alfvén surface ( finishing Alfvén transition ). After this the gas flows out to infinity while undergoing more gradual collimation by the toroidal magnetic field. The optical jet originates as an ordinary stellar wind near the poles of the protostar. Because of the enhancement of the stellar dynamo action associated with circulation currents induced by

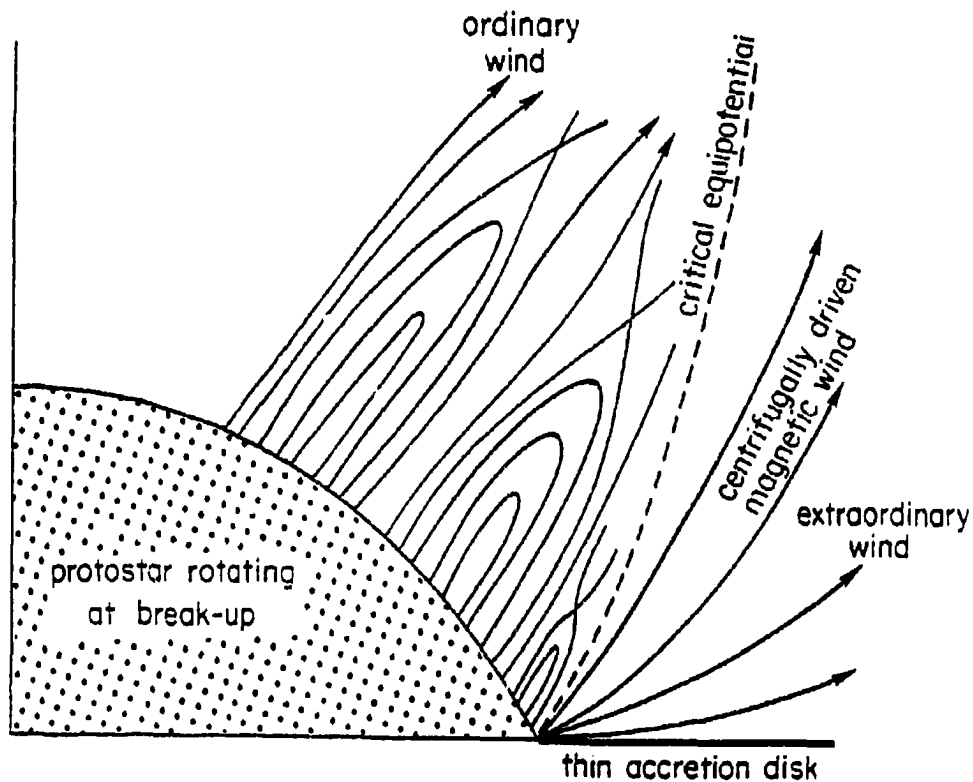


Figure 4. Schematically diagram of the x-celerator protostellar wind model adapted from Shu et al. ( 1988 ). Material enters the star from a thin disk, and the wind leaves from two narrow equatorial bands lying above and below the inflowing matter. The wind is initially launched by the thermal pressure forces. The gas makes a sonic transition near the x-point of the effective gravitational potential. The primary acceleration of the wind occurs magnetocentrifugally between the x-point and the Alfvén surface.

the disk and because of the presence of a more powerful " extraordinary wind " , the ordinary wind has a higher intensity than that of a normal star of the same spectral type and becomes highly collimated in the direction of the rotational poles. This model can explain the predominantly atomic wind seen in HH 7-11 by Lizano et al. ( 1988 ), and the coexistence of a highly collimated ionized jet with a much less well collimated neutral wind in a source like L1551. But there are still many assumptions in this model. One apparent difficulty is that observed stars rotate far more slowly than the model required.

A different variant of the centrifugally driven wind from the disk has been advocated by a number of different groups. Fig. 5a schematically illuminates the basic mechanism of a disk-driven wind model proposed by Pudritz et al ( 1991 ). In this model, the magnetic field lines thread the disk at a radius  $r_0$ , emerge from it, and spread into the disk corona where the magnetic field is nearly force free. The field lines behave dynamically somewhat like rigid wires with the cold gas attached. If the gas is sufficiently cold, then the only forces acting upon it are gravity and the centrifugal force due to the Keplerian rotation of the disk. The centrifugally driven wind commences from the point where the gravitational and centrifugal forces along the magnetic wire are in balance. The magnetic field enforces the corotation of the acceleration gas with the disk until the gas gets to the Alfvén point, after which the gas undergoes a collimation process much like that of stellar driven wind. The optical jet is said to originate at magnetic focal points above and below the hydromagnetic disk ( Fig. 5b ). The disk model appears to provide theoretical answers to the correlation of wind powers and momentum with the luminosity

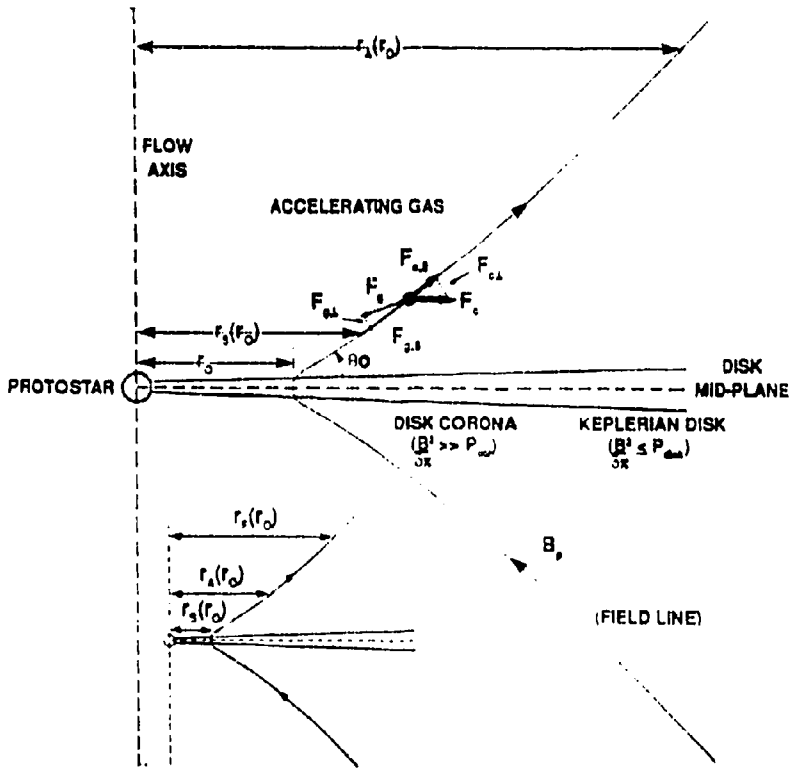


Figure 5a. Schematically structure of a protostellar accretion disk wind model adapted from Pudritz ( 1991 ).

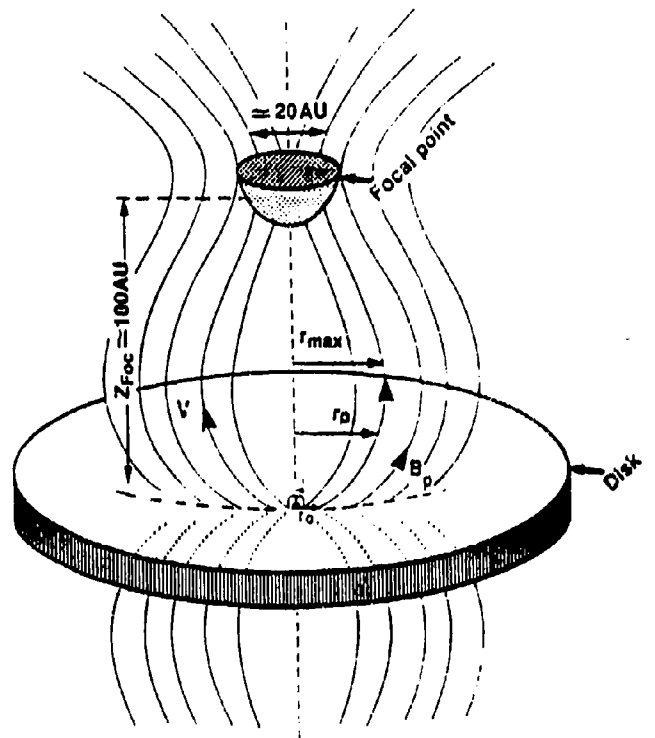


Figure 5b. Optical jets originate at magnetic focal points in the hydromagnetic disk wind taken from Gomez de Castro and Pudritz ( 1990 ).

of the central source. However, the requirement for the disk mass and the magnetic field in the model seems too large.

Historically, most theoretical studies have focused on the production of winds and jets in the context of star formation. There has been very little detailed modeling of the properties of molecular outflow driven by different sorts of winds and jets. In a recent paper, Shu et al. ( 1991 ) calculated the properties of a momentum-conserving outflow in the form of a shell driven by a wide -angle wind. Masson and Chernin ( 1992 ) concluded that molecular outflows cannot be driven in a momentum-conserving fashion by a wide-angle stellar wind, since it tends to sweep up a large quantity of material at the extremities of lobes. In the view of the theoretical difficulties of driving molecular flows with wide-angle winds, there is an increasing interest in the possibility that molecular out flows may be driven only by collimated jets. Recently much work has been done on the properties of the jet-driven molecular outflow by Raga and his collaborators ( 1993a, 1993b ) , and by Masson and Chernin ( 1993, 1994 ). In the models, the molecular outflow corresponds to ambient gas entrained in a turbulent fashion created by the internal jet working surface, rather than simply being pushed forward like a snowplow. Unfortunately, none of these models can be easily tested with currently available observations.

## 2. HH24 Background

The Herbig-Haro objects HH24 lie a few arcminutes south of the reflection nebula

NGC2068 in the Lynds 1630 dark cloud ( the Orion B cloud ) in which star formation has been active for several million years .

One of the closest giant star-formation complexes associated with the Orion complex at a distance of approximately 500 pc ( Maddalena et al.1986 ) , the L1630 cloud contains NGC2064, 2076 2068, 2023, 2024 , and the HH objects HH19 to HH27 ( M78 ) ( Figure 6 ). A 2.2  $\mu\text{m}$  mapping survey toward the L1630 molecular cloud by Strom, Strom and Vrba ( 1976 ) showed one IR source near HH24, later designated as SSV63. Infrared flux measurements by Cohen and Schwartz ( 1983 ) and Cohen et al. ( 1984 ) indicate a bolometric luminosity of 25  $L_{\odot}$  for SSV63. Later IR imaging by Lane ( 1989 ) and Zealey et al. ( 1989 ) has shown that there are probably two additional sources about 8" west and 11.5" northeast of SSV63, which were designated as SSV63W and SSV63NE by Mundt et al. ( 1991 ). Recent large-scale CS mapping of the L1630 cloud in the J = 2-1 line of CS by E. Lada et al. ( 1991a ) indicated that HH24 together with other nearby HH objects is one of the five major dense regions in the L1630 cloud ( figure 7 ). The later near-infrared 2.2  $\mu\text{m}$  survey by E.Lada et al. ( 1991b ) identified four embedded stellar clusters, each probably associated with a CS "clump" except the HH24-26 region. The reason why the HH 24-26 region has fewer infrared sources than the other four major dense regions is still not clear.

The region around HH 24-26 has been mapped using several different tracers of molecular gas. Early observations of the 2 mm  $\text{H}_2\text{CO}$  emission by C.Lada et al. ( 1974 )

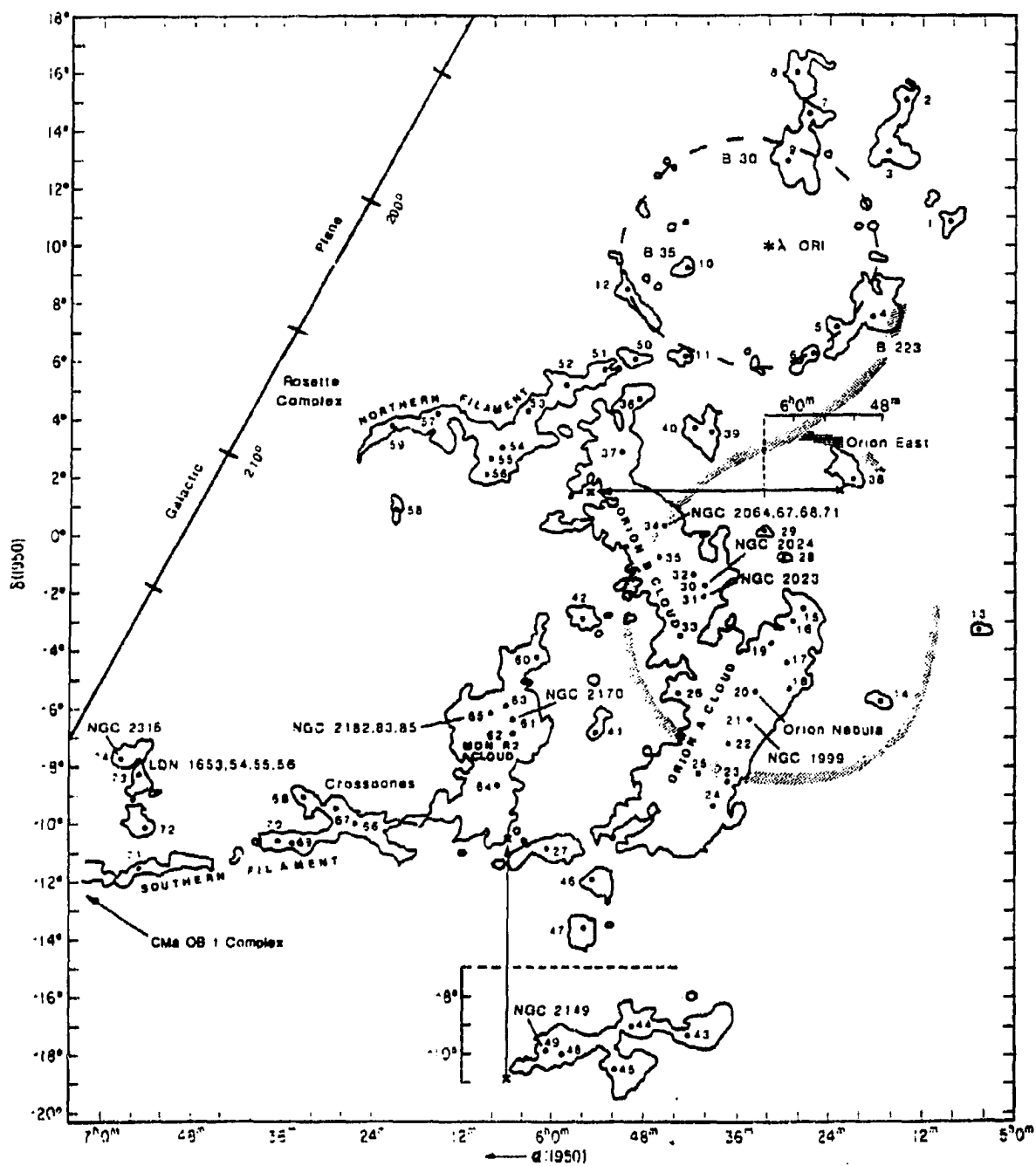


Figure 6. Outlines of large-scale distribution of the molecular cloud complexes in Orion (from the  $^{12}\text{CO}$  mapping by Maddalena et al. 1986).

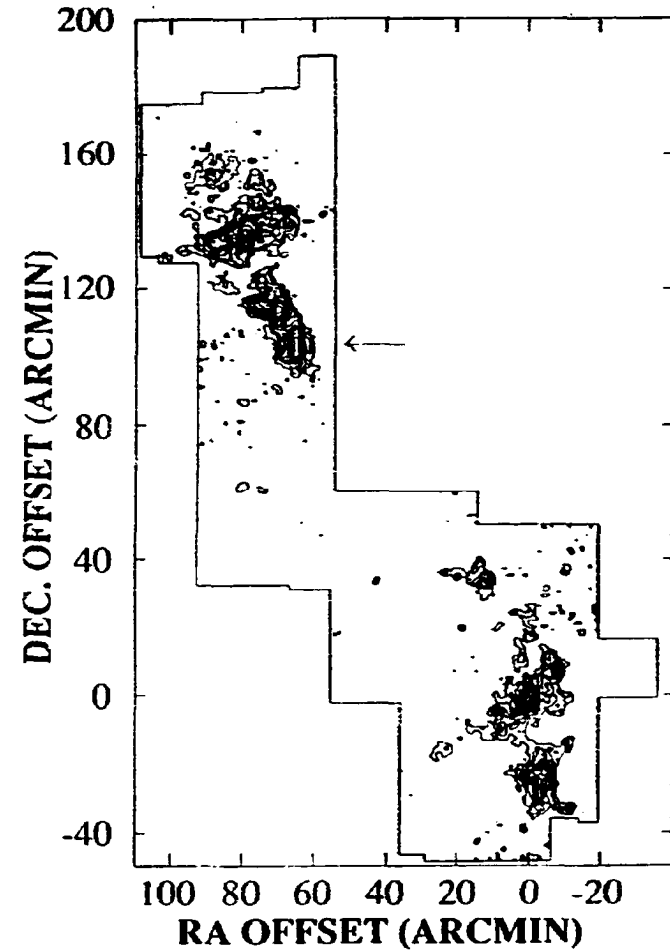
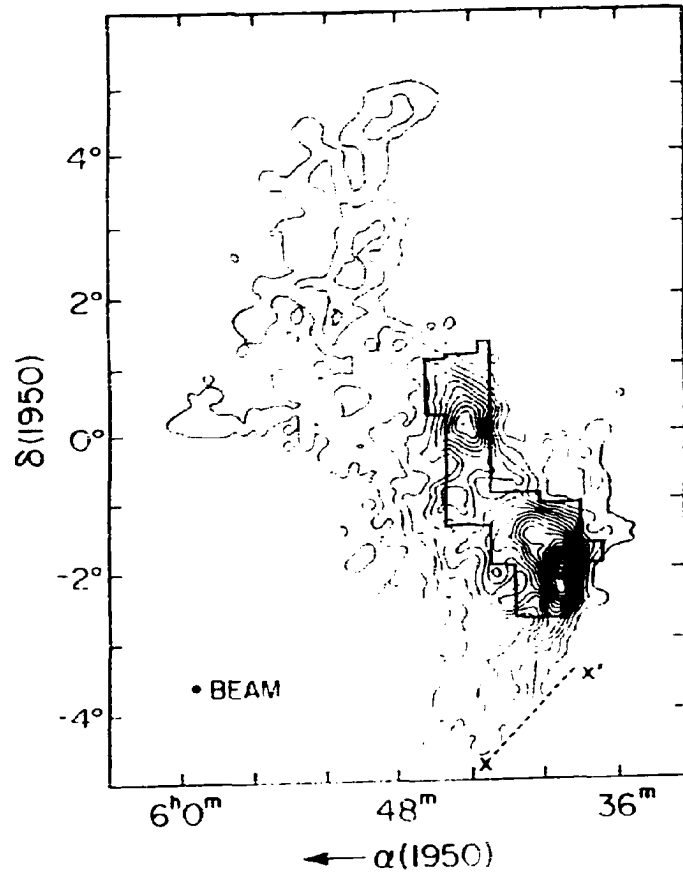


Figure 7. Left (a): contour map of CO emission for the Orion B. The area covered by the CS survey is shown. Right (b): Locations of the embedded infrared clusters and dense CS cores in the Orion B (from E. Lada 1991). The location of HH24 is indicated by an arrow.

showed a rather circular, broad plateau of H<sub>2</sub>CO emission distribution with HH24-26 and the IR star near the center of this dense region ( $n_{\text{H}_2} \sim 10^4 \text{ cm}^{-3}$ ). Strom et al. (1974) found that the typical visual extinction in the dense region was 10-15 magnitude, much greater than the lower limit of 4 magnitudes for the entire L1630 cloud. The ammonia (NH<sub>3</sub>) observations by Matthews et al. (1983) also showed an extended, dense region with the peak near HH24. The extent of the NH<sub>3</sub> emission is somewhat smaller than that of H<sub>2</sub>CO and its shape is narrower in the east-west direction, which appeared to be a disk-like structure. Very recent work by Gibb et al. (1993) in HCO<sup>+</sup> J=4-3 and CS J=5-4 in HH24-26 region showed that the region appears to be clumped. Two of the six clumps are associated with HH24. The observations of <sup>12</sup>CO (J=2-1) by Snell and Edwards (1982, hereafter SE82) revealed the presence of two distinct bipolar outflow systems (see Figure 13). One is centered on HH26 with the infrared source SSV59 identified as the driving source. The other one is centered roughly 2' south of HH24 and none of the known IR sources were identified as the driving source. An additional molecular flow was identified in the vicinity of an H<sub>2</sub>O maser (Haschick et al. 1983) by Edwards and Snell (1984). The recent <sup>12</sup>CO (J=2-1) observation by Gibb et al. (1993) gave a slightly different picture. The red-shifted lobe of SE82 centered on HH26 has been resolved into two separate outflows. The results suggested two parallel bipolar outflows, but there is no clue as to the driving source for the outflows.

HH24 has a particularly complex structure in the optical observations. Figure 8 is



an overview photograph of the HH24 region in [SII] adapted from Mundt et al. ( 1991 ). As can be seen in this figure, HH24 consists of at least six bright knots ( A,B, C, D, E and G in the notation of Jones et al. 1987 ) and perhaps as many as three independent optical outflows ( Mundt 1991, see Fig. 8 ). Among them the jets HH24E and HH24C shows the most prominent structure and is the best-studied. The radial velocity measurements by Solf ( 1987 ) showed that radial velocities of HH24C and HH24E ( called 'F' by Solf ) are nearly equal but have opposite sign ( table I ). Both components are aligned along one axis with the SSV63 located on the axis near the midpoint between them. The proper motion measurements by Jones et al. ( 1987 ) showed HH24C2 appears to emanate directly from SSV63. Combining a radial and proper motion study of HH24C2, Jones et al. ( 1987 ) deduced that the jet is inclined at an angle of  $33^\circ$  relative to the plane of the sky. HH24A was identified as the position of the working surface of the red-shifted jet HH24E, where the jet hits a knot of dense material at the inner edge ( Solf 1987, Jones et al. 1987, Mundt et al. 1991 ). A single source of  $H_2$  emission , interpreted as being due to shock excitation of material at the working surface of the jet, is seen in the near infrared close to HH24A. Mundt et al. ( 1991 ) found some interesting wispy structures associated with each knot of HH24C, which appear to represent shocks driven by the jet into its ambient environment. The second bipolar jet within HH24 connects HH24G and the IR source SSV63NE ( Jones et al. 1987, Mundt et al. 1991 ). HH24G, which apparently emanates from SSV63NE, represents the blue-shifted jet. The red-shifted counterjet is still uncertain. HH24G consists of three major knots G1, G2 and G3. A further study by Mundt et al. showed that G1 and G2 appear to contain a complex group of sub-

condensations, which indicate that the internal shock structure in the jet is very chaotic. The inclination of the jet relative to the plane of the sky is unknown since HH24G is too faint for the measurement of proper motion. The IR source SSV63W appears to give rise to a third bipolar jet traced by several faint knots ( Mundt et al. 1991 ). Due to the faintness of the knots, no radial velocity or proper motion has been measured for these knots. It should be noted that not all emission knots can be easily explained in terms of the three bipolar jets. The radial velocity and proper motion measurements by Solf ( 1987 ) and Jones et al. ( 1987 ) are summarized in Table I.

Table I  
Positions and Kinematics Data for HH24

Knots	Position <sup>b</sup>		Radial Velocity $V_r$ ( $\text{km s}^{-1}$ )	Proper Motion <sup>b</sup>	
	$\alpha$ (1950)	$\delta$		$\mu_x$	$\mu_y$ ( $\text{arcsec cent}^{-1}$ )
A	5 <sup>h</sup> 43 <sup>m</sup> 35 <sup>s</sup> .66	-0° 11' 31".4	47 <sup>a</sup>	-1.4±0.5	0.8±1.0
B	5 43 34.44	-0 11 11.7	-9 <sup>a</sup>	-0.2±0.2	0.8±0.2
C2	5 43 34.15	-0 10 56.5	-142 <sup>a</sup>	-6.6±0.7	13.1±1.3
D	5 43 36.39	-0 11 0.4	60 <sup>a</sup>	3.5±3.6	0.8±6.2
E	-----	-----	164 <sup>a</sup>	-----	-----
G1	-----	-----	-133 <sup>c</sup>	-----	-----

<sup>a</sup> Solf ( 1987 )  $H_{\alpha}$  line with respect to background velocity  $V_{LSR} = 11 \text{ km s}^{-1}$

<sup>b</sup> Jones et al. ( 1987 )

<sup>c</sup> Heliocentric radial velocity ( Jones et al. 1987 )

## II. Observations

Observations in  $^{12}\text{CO}$  J=3-2,  $^{12}\text{CO}$  J=2-1 and  $^{13}\text{CO}$  J=2-1 were made using the 15m James Clark Maxwell Telescope ( JCMT ) on Manna Kea, Hawaii, during a run in August 1993 by G.F. Mitchell, T.I. Hasegawa and the author.

A hybrid autocorrelation spectrometer covering a bandwidth of 250 MHz ( one of its bandwidths ) with a spectral resolution of 378 kHz (  $0.33 \text{ km s}^{-1}$  ), together with a single-channel SIS receiver ( B3i which covers a band from 298 to 380 GHz ), were employed for  $^{12}\text{CO}$  J=3-2. The receiver temperature ranged from 181K to 215K and the system temperature from 638K to 704K. The same spectrometer backends along with a single-channel SIS receiver ( A2, cover a band from 218 to 280 GHz ) was employed for  $^{12}\text{CO}$  J=2-1 and  $^{13}\text{CO}$  J=2-1. The receiver temperature was 84K to 100K and the system temperature was 390K to 406K. Calibration of the spectral line as done via cold ( liquid nitrogen ) and ambient loads by using the standard chopper wheel method. Data were taken in a position-switching mode with a reference position 10' to 20' from the center of the source. Measurements of N2071IR were used to determine the half-power beam width ( HPBW ) and the main beam efficiency (  $\eta_{\text{mb}}$  ) for a spatially extended source much larger than the main beam. For  $^{12}\text{CO}$  J=2-1 and  $^{13}\text{CO}$  J=2-1, the resulting values are  $\text{HPBW}=20''.8$ ,  $\eta_{\text{mb}}=0.72$ . For  $^{12}\text{CO}$  J=3-2,  $\text{HPBW}=14''.3$ ,  $\eta_{\text{mb}}=0.53$ . Line intensities are presented as antenna temperatures (  $T_{\text{A}}^{\bullet}$  ) which have been corrected for

the atmosphere, ambient temperature, telescope losses, and forward spillover and scattering (  $\eta_{fs}$  ).

The  $^{12}\text{CO}$  J=3-2 spectra , obtained at 254 positions with a 10" spacing are shown in Figure 9.  $^{12}\text{CO}$  J=2-1 and  $^{13}\text{CO}$  J=2-1 spectra were taken toward 6 selected positions that showed particularly broad wings( Fig. 10 ). The coordinates ( epoch 1950 ) for the central position (  $\Delta\alpha$  ,  $\Delta\delta$  ) = ( 0,0 ) are  $\alpha = 5^{\text{h}} 43^{\text{m}}34.7^{\text{s}}$ ,  $\delta = -00^{\circ}11'10''$ .

All data reduction was carried out using the SPECX package. Table II summarizes the observational parameters.

Table II  
Observational Parameters

Transition	Frequency ( Ghz )	$\Delta v^a$ ( km s <sup>-1</sup> )	Beam size <sup>b</sup> ( arcseconds )	$\eta_{mb}^c$	RMS <sup>d</sup> ( K )
<sup>12</sup> CO J=2-1	230.5380	0.407	20.8"	0.72	0.138
<sup>13</sup> CO J=2-1	220.3987	0.426	20.8"	0.72	0.061
<sup>12</sup> CO J=3-2	345.7960	0.271	14.3"	0.53	0.204

<sup>a</sup> Velocity resolution in km s<sup>-1</sup>

<sup>b</sup> Half-power beam width ( HPBW )

<sup>c</sup> Main beam efficiency

<sup>d</sup> Typical rms noise level

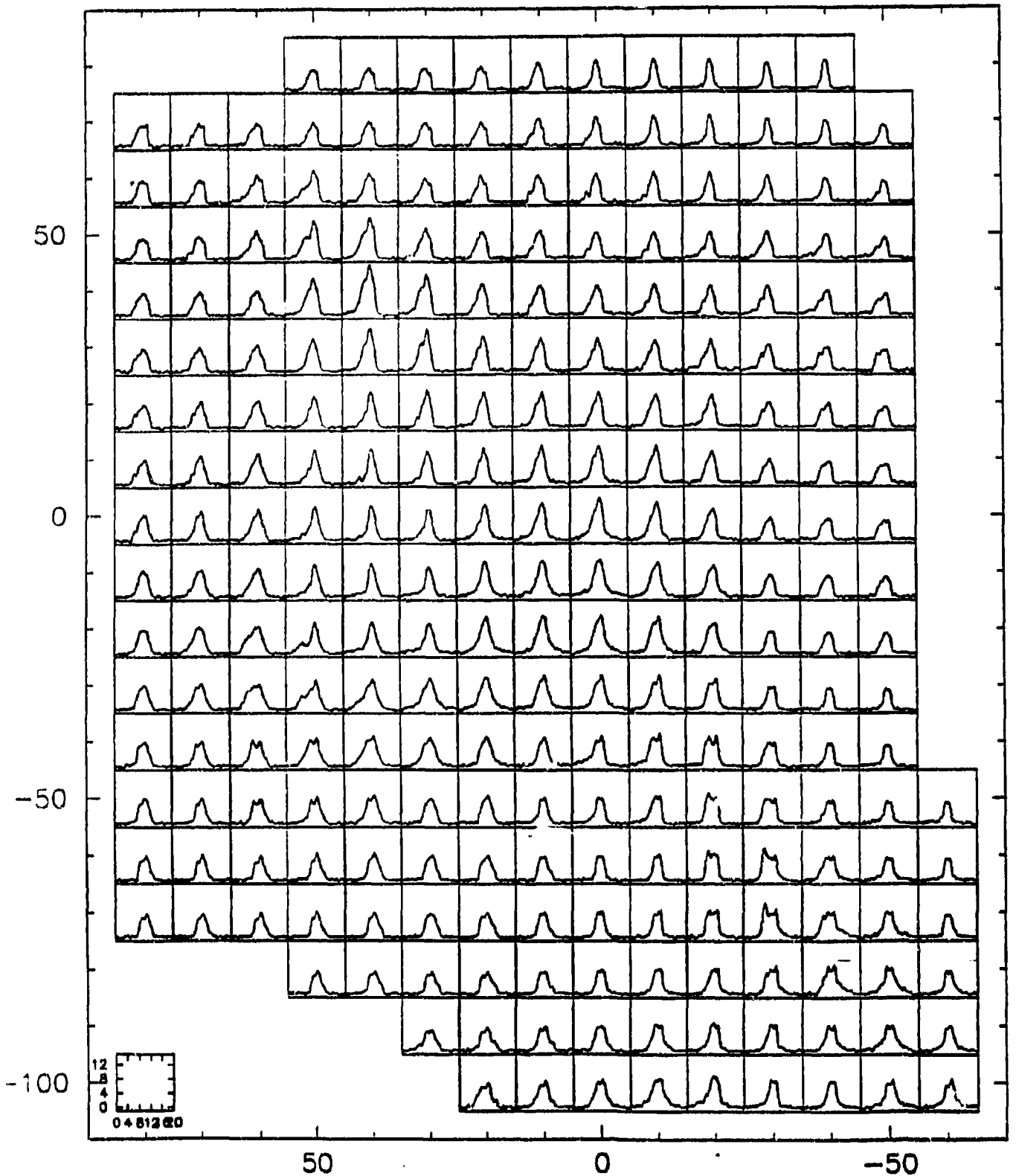


Figure 9. A  $^{12}\text{CO}$  J=3-2 map of 254 spectra ( antenna temperature vs. LSR velocity ) on a  $10''$  grid spacing. The positions are given as R.A. and DEC. offset (  $\Delta\alpha$ ,  $\Delta\delta$  ) expressed in arcseconds from the map center (  $\alpha = 5^{\text{h}} 43^{\text{m}} 34.7^{\text{s}}$ ,  $\delta = -00^{\circ} 11' 10''$  ). North is to the top and East is to the left.

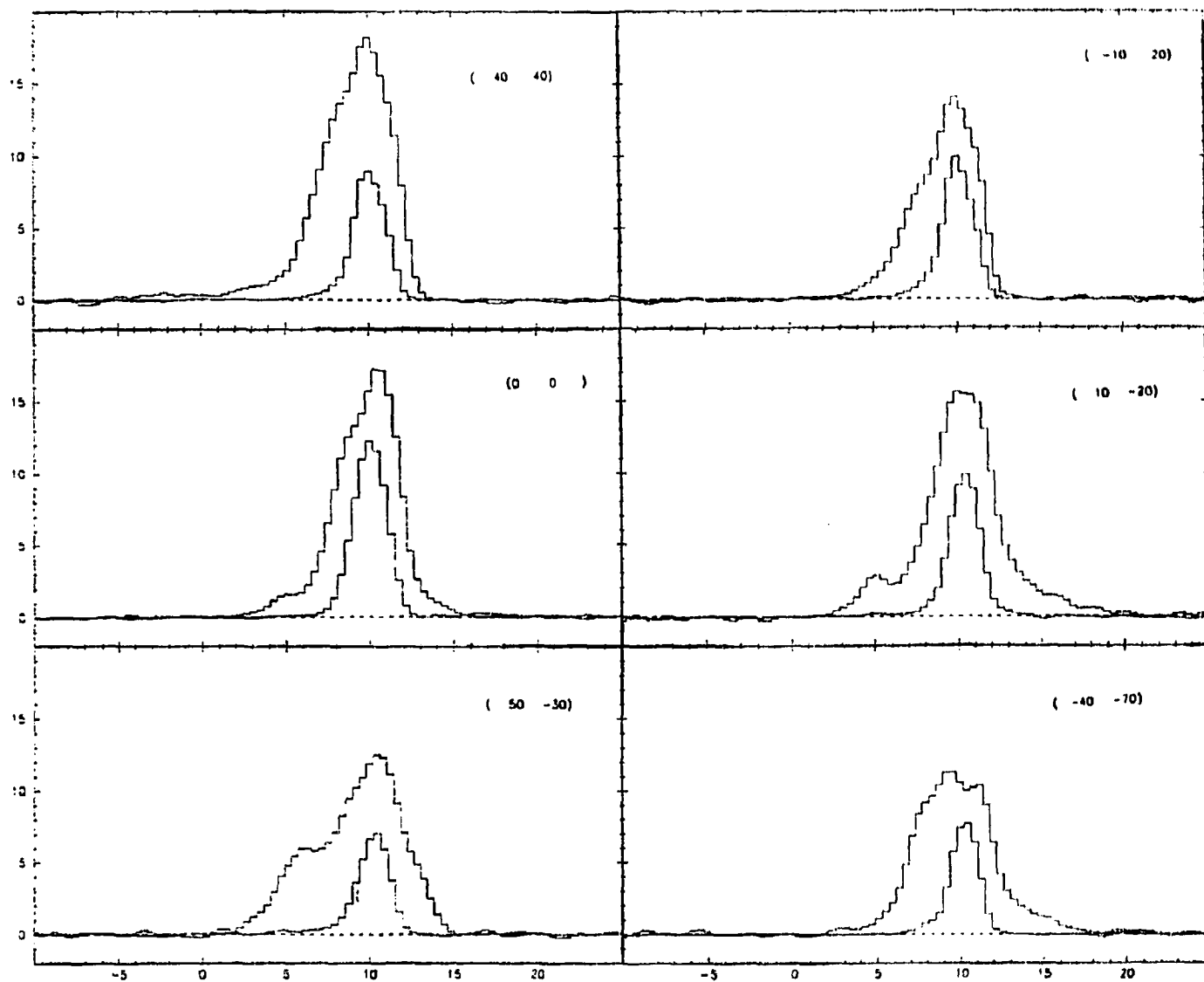


Figure 10.  $^{12}\text{CO}$  J=2-1 and  $^{13}\text{CO}$  J=2-1 spectra at 6 selected positions. The weaker line is  $^{13}\text{CO}$  J=2-1. The positions are given as R.A. and DEC. offset ( $\Delta\alpha$ ,  $\Delta\delta$ ) in the right hand.

### III. Results of the Observations

The high resolution 254 point map of  $^{12}\text{CO}$  J=3-2 emission in this region revealed a complex distribution of molecular gas with the full velocity extent of the emission profile ranging from  $18 \text{ km s}^{-1}$  at the position ( 40, 40 ) and ( 0,0 ) to  $6 \text{ km s}^{-1}$  at the northeast boundary of the map.

The observations of  $^{13}\text{CO}$  J=2-1 ( Fig. 10 ) show a peak velocity at  $V_{\text{LSR}}=10.2 \text{ km s}^{-1}$  and a local standard of rest velocity range from  $8.5$  to  $11.8 \text{ km s}^{-1}$ . We adopt  $V_{\text{LSR}}=10.2 \text{ km s}^{-1}$  as the velocity of the "ambient" component of this region. This is in good agreement with the results of  $10 \text{ km s}^{-1}$  obtained by Snell and Edward ( SE82 ) for  $^{13}\text{CO}$  J=1-0 ,  $11 \text{ km s}^{-1}$  obtained by Solf ( 1987 ) from  $\text{H}\alpha$  and forbidden lines, and  $10.2 \text{ km s}^{-1}$  obtained by Lada ( 1974 ) from  $\text{H}_2\text{CO}$  observations. To distinguish the high-velocity and low-velocity portions of the profiles, we define the inner and outer wings for both redshifted and blueshifted emissions by examination of the  $^{13}\text{CO}$  J=2-1 and  $^{12}\text{CO}$  J=2-1 spectra. At any position the boundary between inner and outer wings is defined as the largest velocities at which the  $^{13}\text{CO}$  emissions can be detected. Thus, in the outer wing,  $^{12}\text{CO}$  is detectable but  $^{13}\text{CO}$  is not.

Representative spectra of  $^{12}\text{CO}$  J=3-2 obtained towards SSV63 and in the vicinity of SSV63NE and SSV63W [positions ( 0, 0 ), ( 10,10 ), and( -10, -10 ), respectively ] are

shown in Figure 11. Also shown are a  $^{12}\text{CO}$  J=2-1 spectrum and a  $^{13}\text{CO}$  J=2-1 spectrum at position ( 0,0 ). The J=3-2 spectrum at position ( 0,0 ) is slightly asymmetric, the blue wing being more pronounced than the red wing at low velocities. The velocity extent for both the blue and red wings is limited to  $\pm 9 \text{ km s}^{-1}$  from the line center. The J=3-2 spectra at positions ( 10, 10 ) and ( -10, -10 ) are similar to that at position ( 0,0 ) with a total velocity extent of  $14 \text{ km s}^{-1}$ . The red wing is broader at position ( -10, -10 ) than at position ( 10, 10 ), while the reverse is true for the blue wing.

Figure 12 shows  $^{12}\text{CO}$  J=3-2 spectra taken at positions ( 40,40 ), ( 50,50 ), ( 60,60 ) and ( 70,70 ) along a line from SSV63NE to the north-east through HH24G. The feature HH24G extends from ( 40,40 ) to ( 60,60 ). The  $^{12}\text{CO}$  blue-shifted emission at the positions shows striking correlation with the HH24G jet. A  $^{12}\text{CO}$  J=2-1 and a  $^{13}\text{CO}$  J=2-1 spectrum obtained at the position ( 40, 40 ) are also shown in this figure ( bottom ). The spectra are asymmetric, with very broad and prominent blue wings. At position ( 40,40 ), the blue wing reaches  $15 \text{ km s}^{-1}$  from the line center velocity, whereas the red wing has a velocity extent of only  $5 \text{ km s}^{-1}$ . At positions ( 50, 50 ), ( 60, 60 ), and ( 70, 70 ), the spectra reveal interesting complexity with additional emitting components. This complexity may be the result of the superposition of several velocity components. Both the line peak intensity and the blue wing intensity decrease toward the north-east from the position ( 40, 40 ), as does the velocity extent of the blue wing.

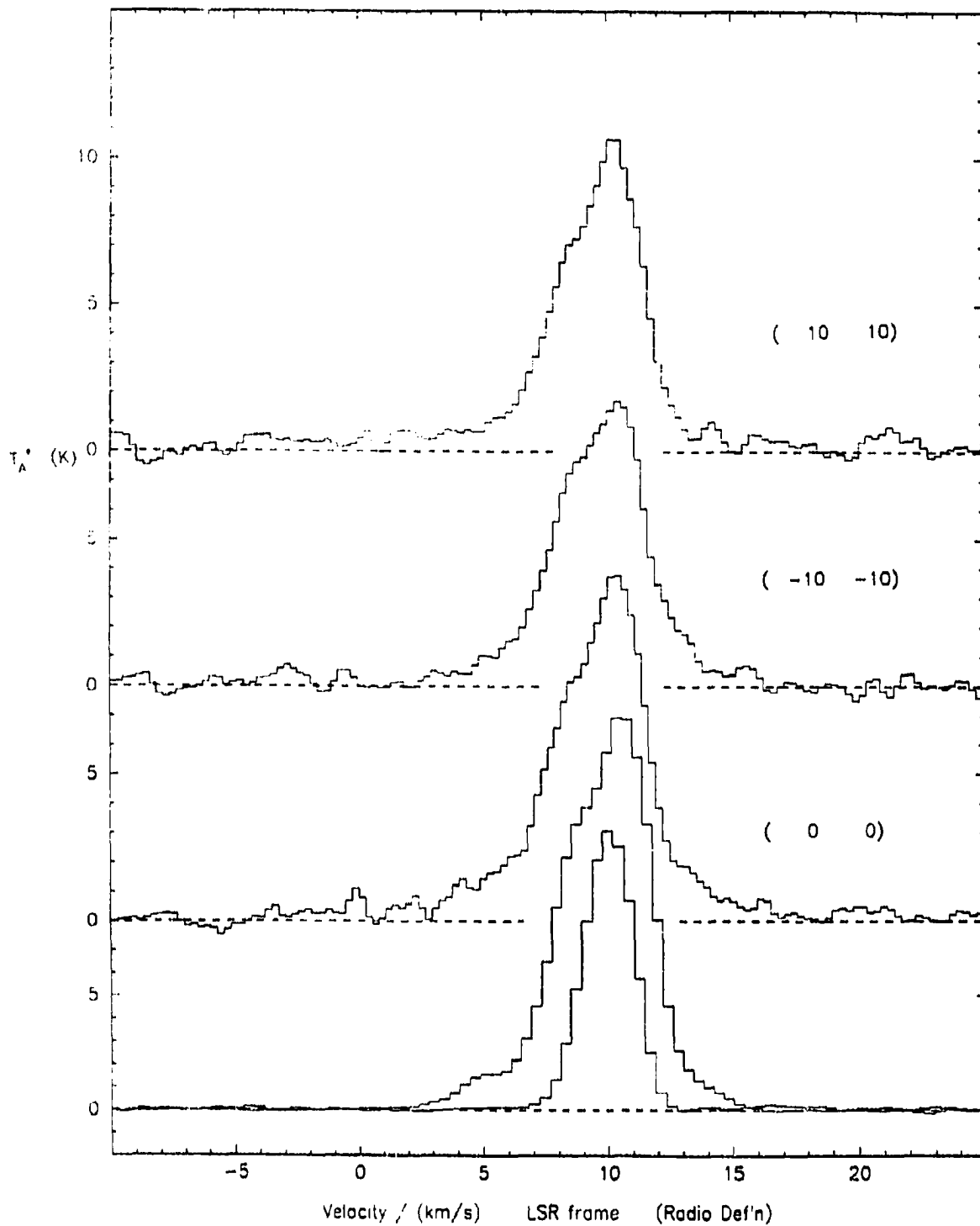


Figure 11. Selected  $^{12}\text{CO}$  J=3-2 towards SSV63, in the vicinity of SSV63NE and SSV63W at positions  $(0,0)$ ,  $(10,10)$  and  $(-10,-10)$ . Also shown are a  $^{12}\text{CO}$  J=2-1 spectrum and a  $^{13}\text{CO}$  J=2-1 spectrum at position  $(0,0)$ .

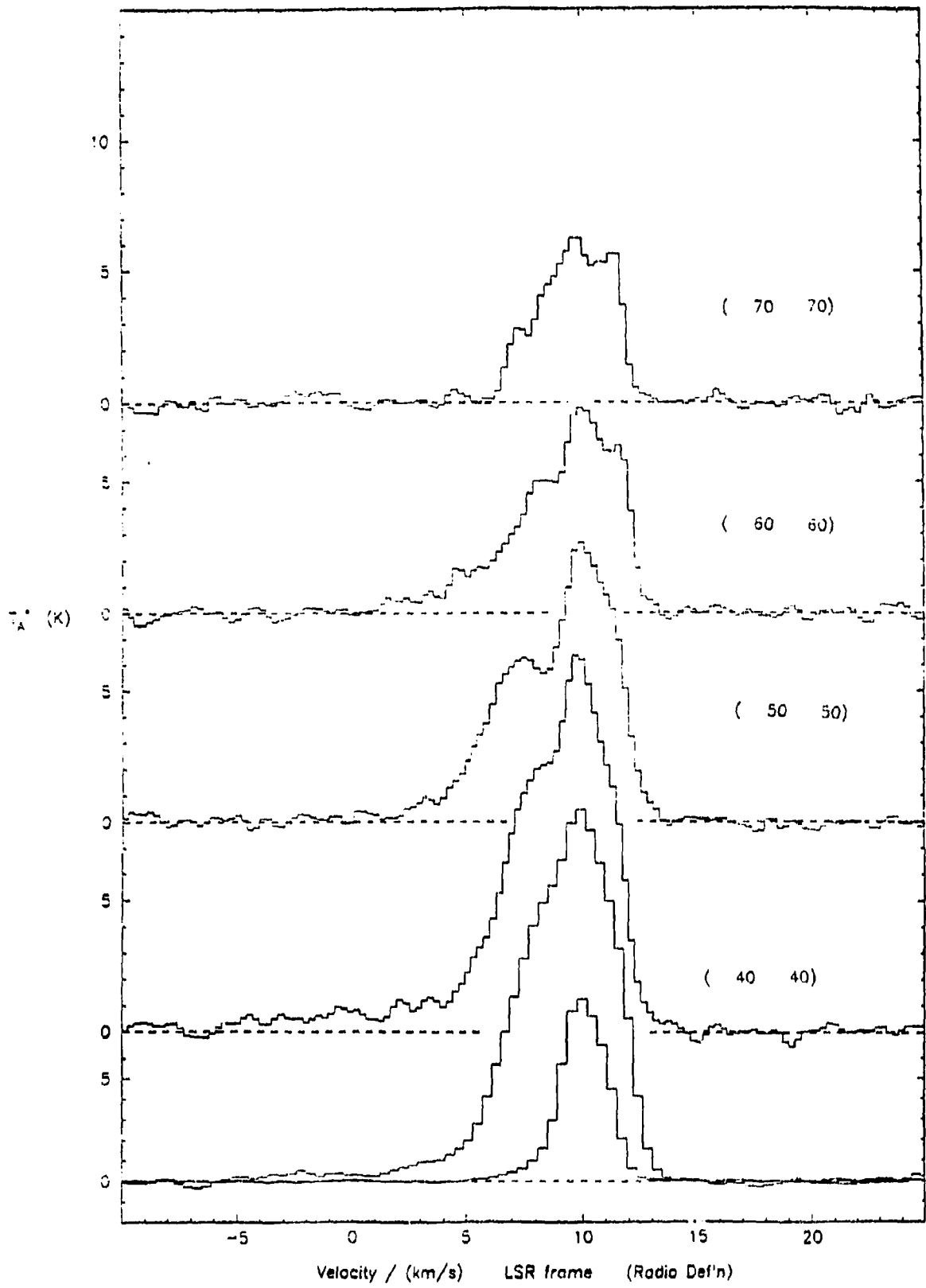


Figure 12. Four  $^{12}\text{CO}$   $J=3-2$  spectra, one  $^{12}\text{CO}$   $J=2-1$  spectrum and one  $^{13}\text{CO}$   $J=2-1$  spectrum at positions (40,40), (50,50), (60,60) and (70,70). The (40,40) position is near a peak in the integrated intensity of blueshifted outflow gas which is coincident with the HH24G jet.

## HH 24-27 AND HH 1-2

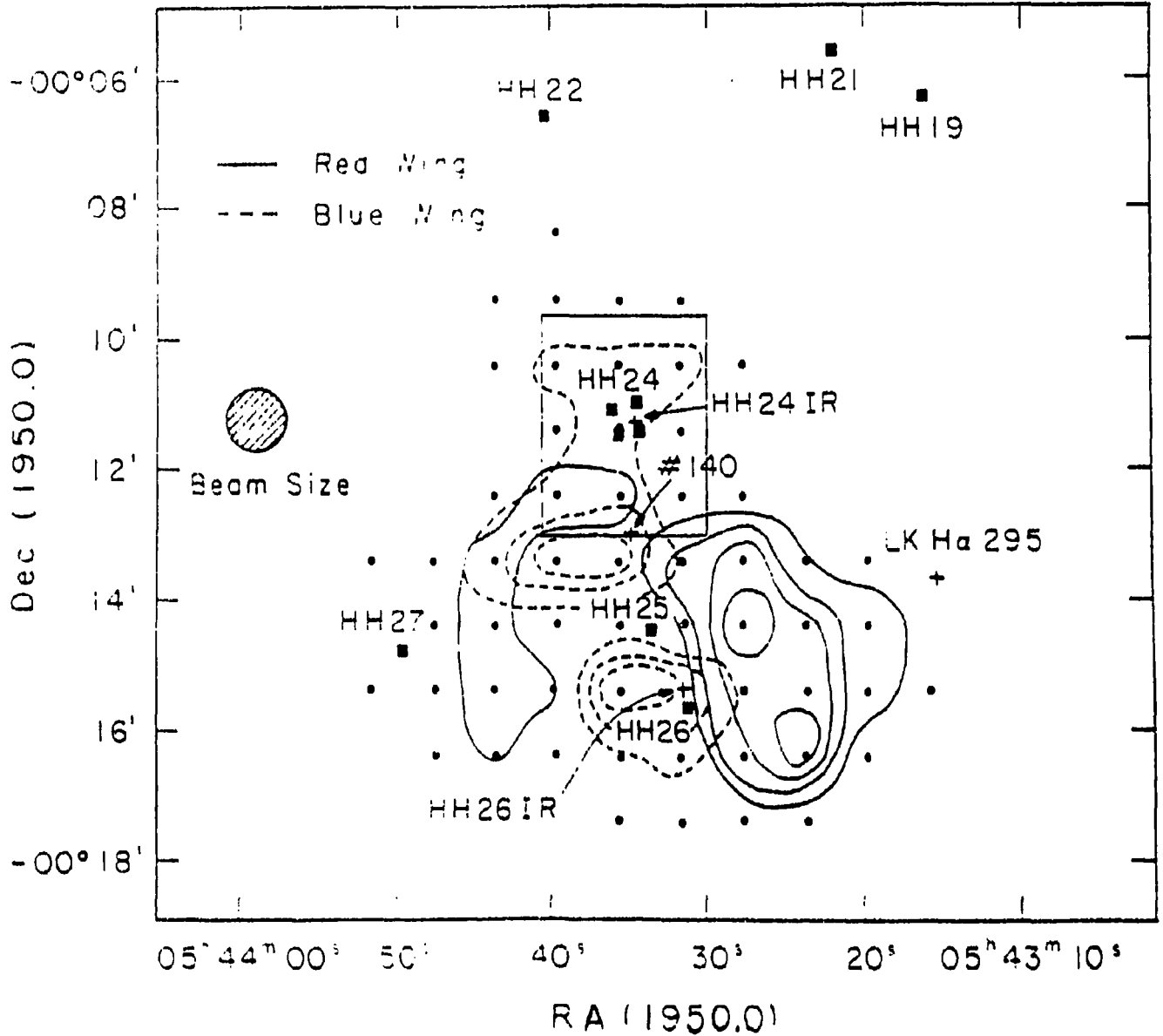


Figure 13. The large scale  $^{12}\text{CO}$  contour map of SE82 in the HH24-26 region. The spatial coverage of the  $^{12}\text{CO}$  J=3-2 observations in the present study are shown as a box.

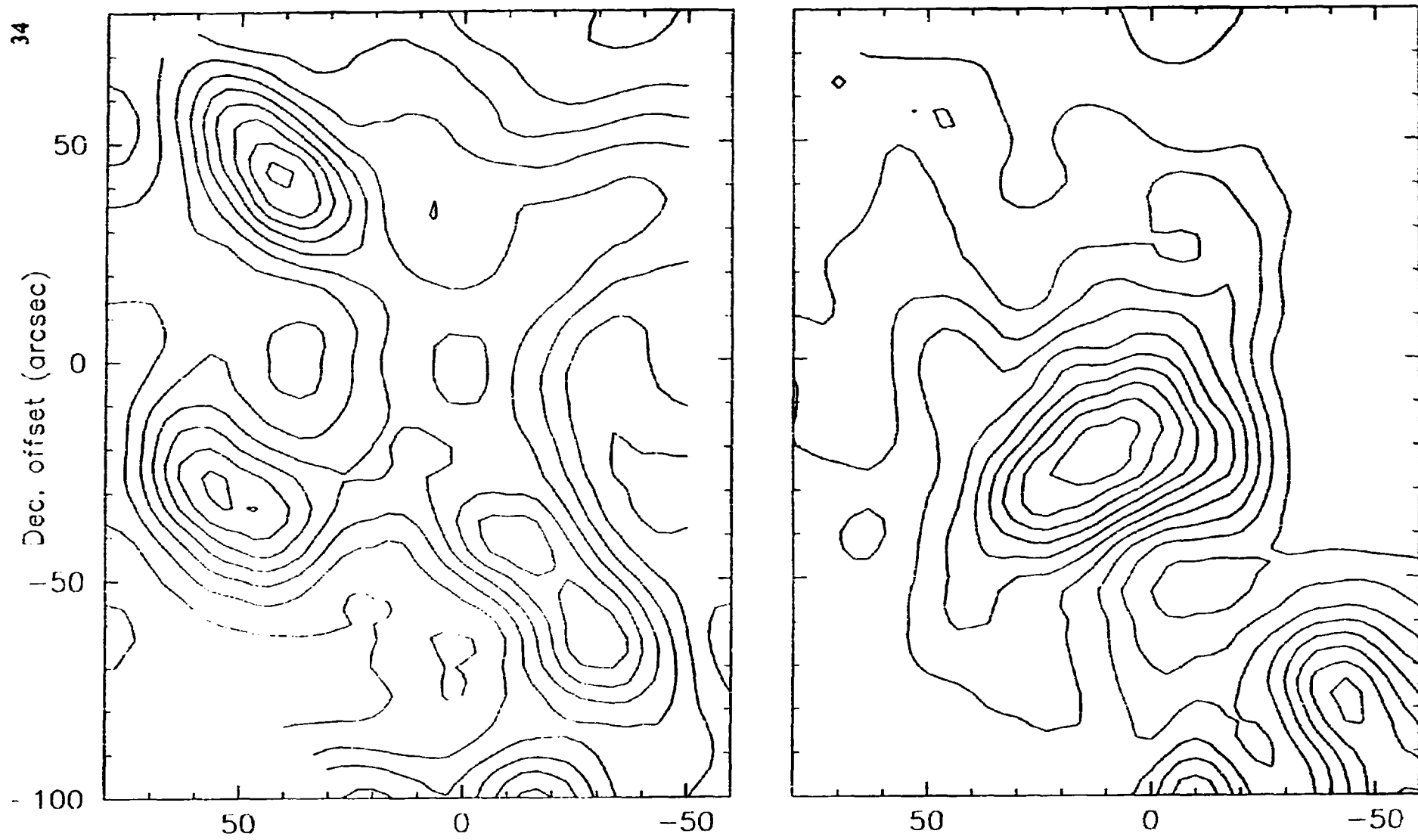


Figure 14. ( Caption is on the back )

The large scale  $^{12}\text{CO}$  mapping of the HH24-26 region by SE82 identified two possible outflows. The spatial coverage of the  $^{12}\text{CO}$  J=3-2 observations in the present study are shown as a box superposed on the contour map of SE82 in Figure 13. The present higher resolution observations reveal a more complex morphology. Figure 14 shows maps of the total integrated intensity of red-shifted and blue-shifted gas. The blue-shifted emission is integrated from  $-4 \text{ km s}^{-1}$  to  $8 \text{ km s}^{-1}$ , and the red-shifted emission is integrated from  $12$  to  $20 \text{ km s}^{-1}$ . From the maps ( Figure 13 and 14 ) it is clearly seen that the part of the single blue-shifted lobe of SE82 near HH24 has been resolved into multiple outflow lobes.

Channel maps, which show the detailed spatial-velocity distributions of the gas, are presented in Figure 15. Each panel covers a velocity width of  $1 \text{ km s}^{-1}$ . For each velocity range the top figure shows contours only, while the bottom figure includes a greyscale plot. Figure 15 covers a velocity range from  $-4$  to  $20 \text{ km s}^{-1}$ . In each map the lowest contour-level has been chosen to be not lower than  $3 \sigma$  ( rms ) noise level (  $1\sigma = 0.106 \text{ K-km s}^{-1}$  ). Figure 15 a-l represent the distribution of the blue component for the velocity range from  $-4 \text{ km s}^{-1}$  to  $8 \text{ km s}^{-1}$ . Figure 15 m-p correspond to the velocity range of the ambient molecular cloud ( from  $8 \text{ km s}^{-1}$  to  $12 \text{ km s}^{-1}$  ). These maps are dominated by emission from the ambient molecular cloud. Figure 15 q-x show the distribution of the red component for the velocity range from  $12 \text{ km s}^{-1}$  to  $20 \text{ km s}^{-1}$ . Figure 15 shows that the

distribution of the gas with the largest velocities relative to the ambient gas velocity is strongly clumped.

The blue-shifted maps show that there are four major distinct elongated blue lobes pointing to the map center. Two straight lines pass through the peaks of the four major lobes : one lies in a northeast-southwest direction and the other one in a northwest-southeast direction. The two lines intersect at a point very close to the map center. The two outflow patterns are seen most clearly in Figure 15h and Figure 15k. Two peaks of blueshifted emission marked as B3 and B4 can be identified in the northwestern part of the map. The peaks marked B1 at position ( 40, 50 ) and B2 at position ( -30 -60 ) are located at the edges of the northeast-southwest. The northwest-southeast axis threads through the peaks B3 and B4 at positions ( -20, 20 ) and ( -40, 40 ) and peak B5 at position ( 40, -30 ). Peaks B3 and B4 extend to the northwest direction and probably beyond the mapped region. With increasing velocity, lobe B2 is resolved into two distinct lobes B21 and B22 ( see Fig. 15h ) and the other clumps become more and more detached from each other. Lobe B1 has a broad velocity range persisting through the whole blue velocity interval. The lobes marked B3 and B4 in Figure 15h only appear at limited velocity range from  $V_{LSR}=2 \text{ km s}^{-1}$  to  $5 \text{ km s}^{-1}$ . The length to width ratio of the peak B1 is approximately 3 implies that the blue emission flow is well collimated. The two axes do not exactly go through any of the IR sources but lie within 10" from them, an offset smaller than the beam size.

The red-shifted  $^{12}\text{CO}$  emission appears to consist of two spatial components ( hereafter referred to as R1 and R2 ). A component ( R1 ) at position ( 15, -20 ) is seen positionally close to the blue-shifted peaks at ( 50,-30 ), ( -10,-40 ) and ( 0,0 ), but its peak position exactly corresponds to a depression of blue emission ( see Fig. 15g and 15u ). It is interesting to note that the peak of R1 is spatially coincident with the red-shifted HH24A which represent the working surface of the red-shifted HH24E jet ( Fig. 16 ). The second component ( R2 ), at position ( -40,-80 ) is elongated and closely aligned to the axis defined by the blue lobe B1. R2 extends to the southwest beyond the mapped region. The good alignment of R2 and lobe B1 along the northeast-southwest line suggests that they are the blue and red lobes of a single outflow. SSV63NE is likely the driving source. We do not find a good candidate for the red-shifted counterpart of the blue gas along the NW-SE direction. We suspect that R2 might be the red counterpart, however its peak location is offset from the NW-SE axis.

The emission near the ambient gas velocity ( Figs. 15m-p ) shows an emission peak near the position of the strongest red-shifted peak ( R1 ) and a second peak at the position of the strongest blue-shifted peak ( B1 ). It appears that the outflows significantly contribute to the observed emission even at the ambient gas velocity.

Among the features observed in the outflow gas, the most remarkable is perhaps the coincidence of the lobe B1 with the optical jet traced by HH24G. HH24G passes exactly through the center of the lobe B1. This is evident in Figure 17 and Figure 18 in

which the map of the integrated intensity of blue-shifted emission from  $2 \text{ km s}^{-1}$  to  $5 \text{ km s}^{-1}$  is overlaid on a CCD picture of the [ SII ] emission observed by Mundt et al. ( 1991 ). However the axis traced by peaks B3, B4 and B5 is not well aligned with any of the optical jets but is rotated by 20 degrees with respect to the optical jet traced by HH24C and HH24E and is parallel to the optical jet traced by several faint knots with a few arcsecond distance. The features will be discussed further in Part V.

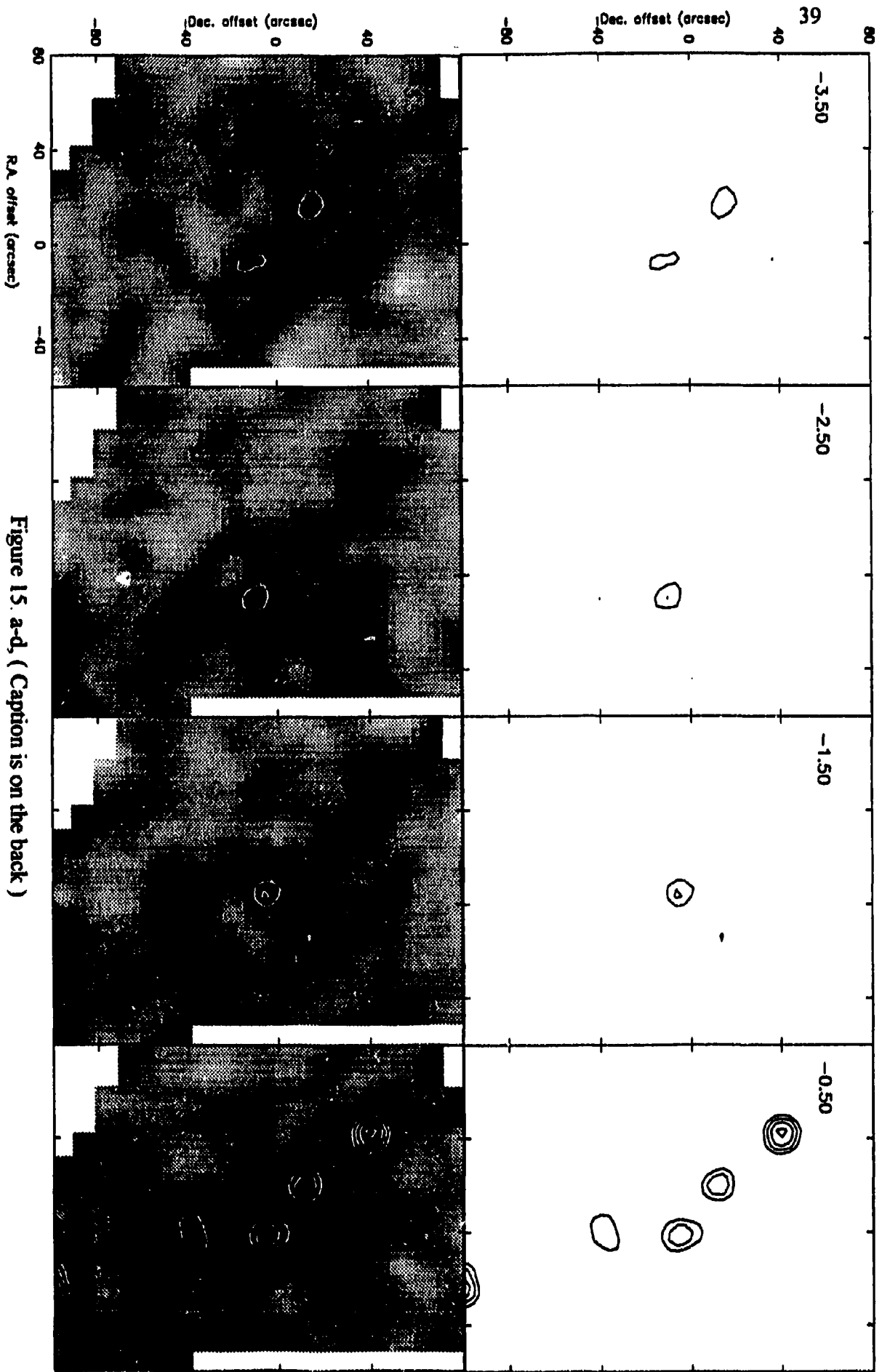


Figure 15. a-d, ( Caption is on the back )

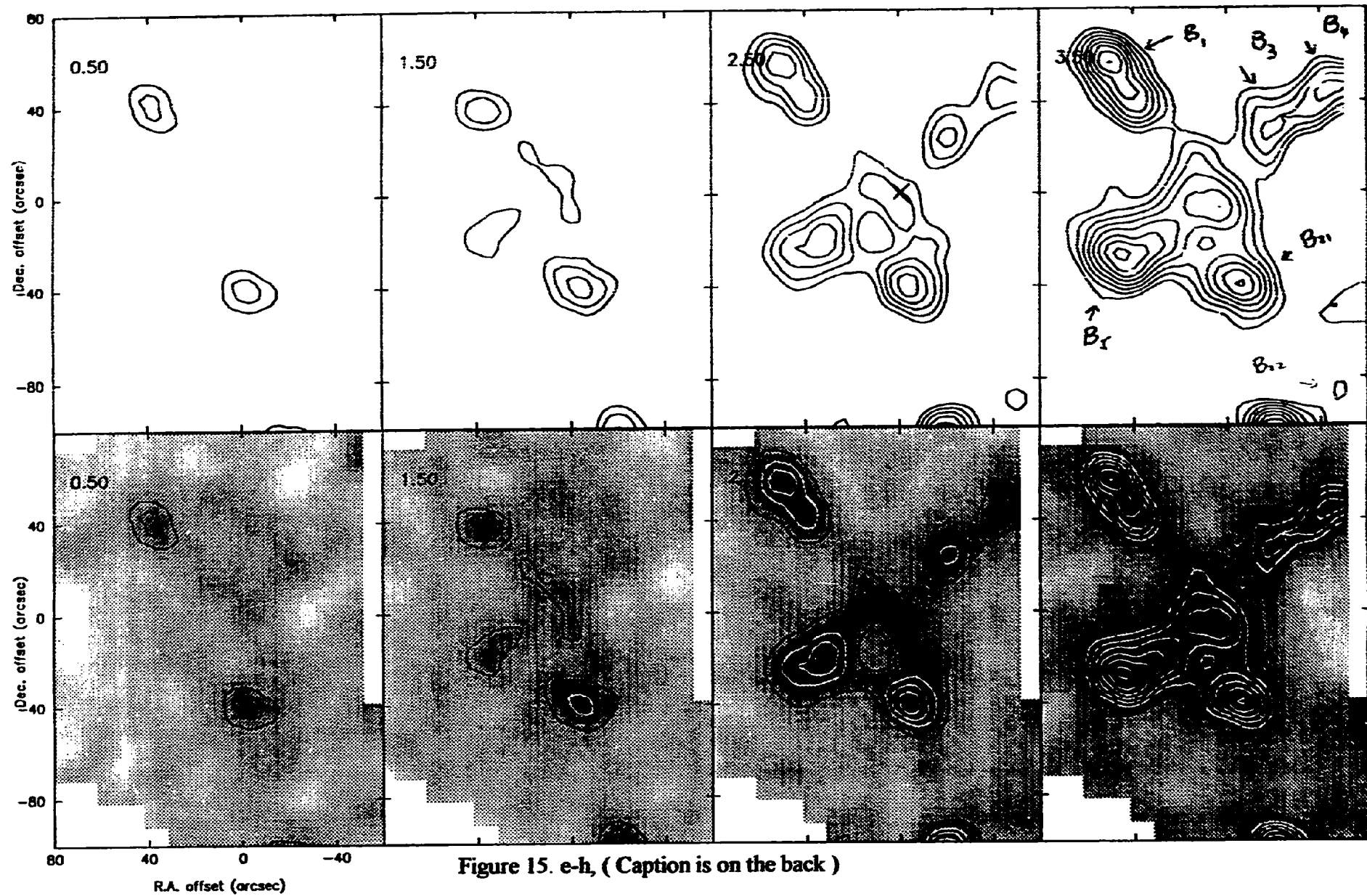


Figure 15. e-h, ( Caption is on the back )

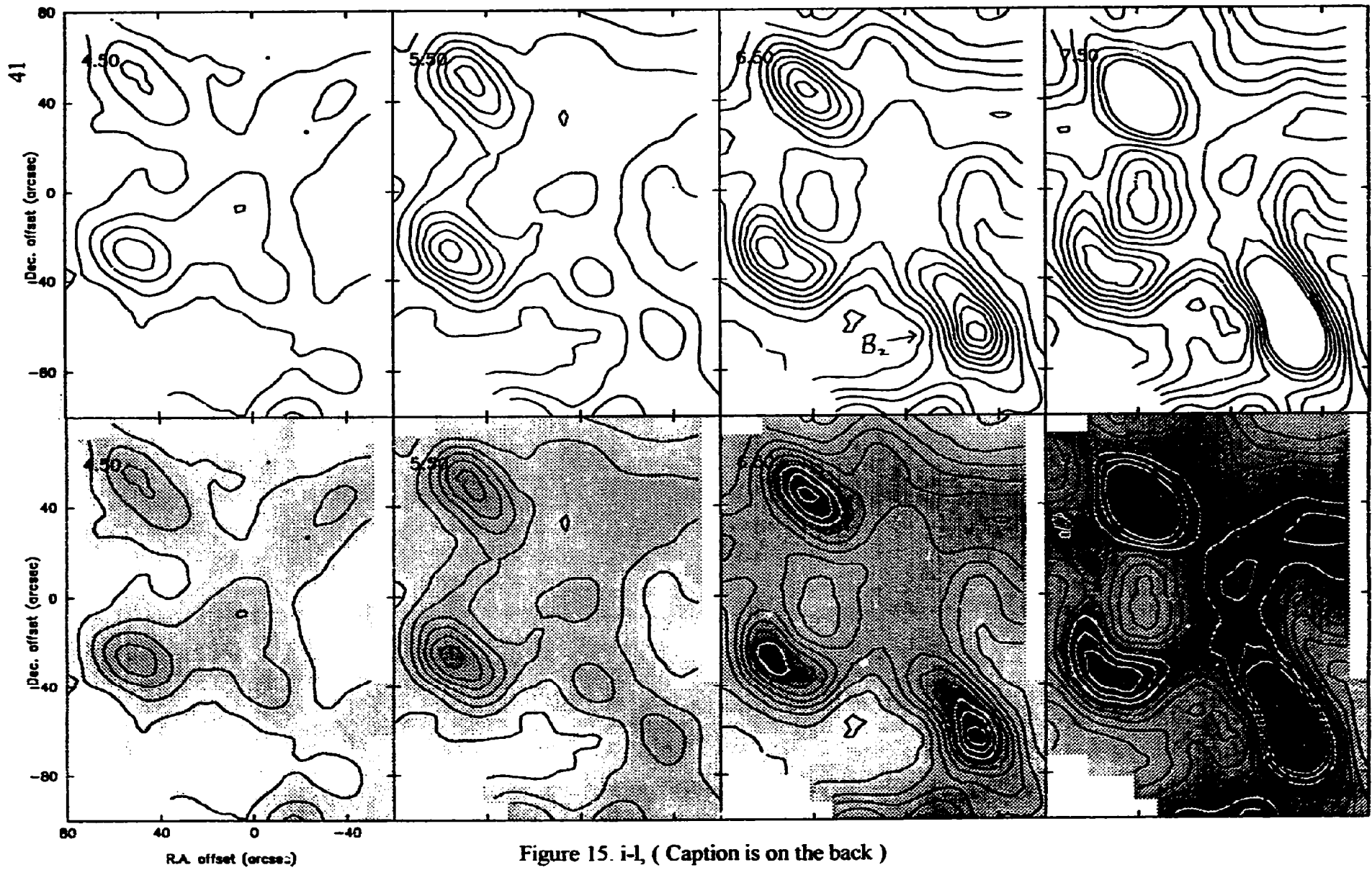


Figure 15. i-1, ( Caption is on the back )

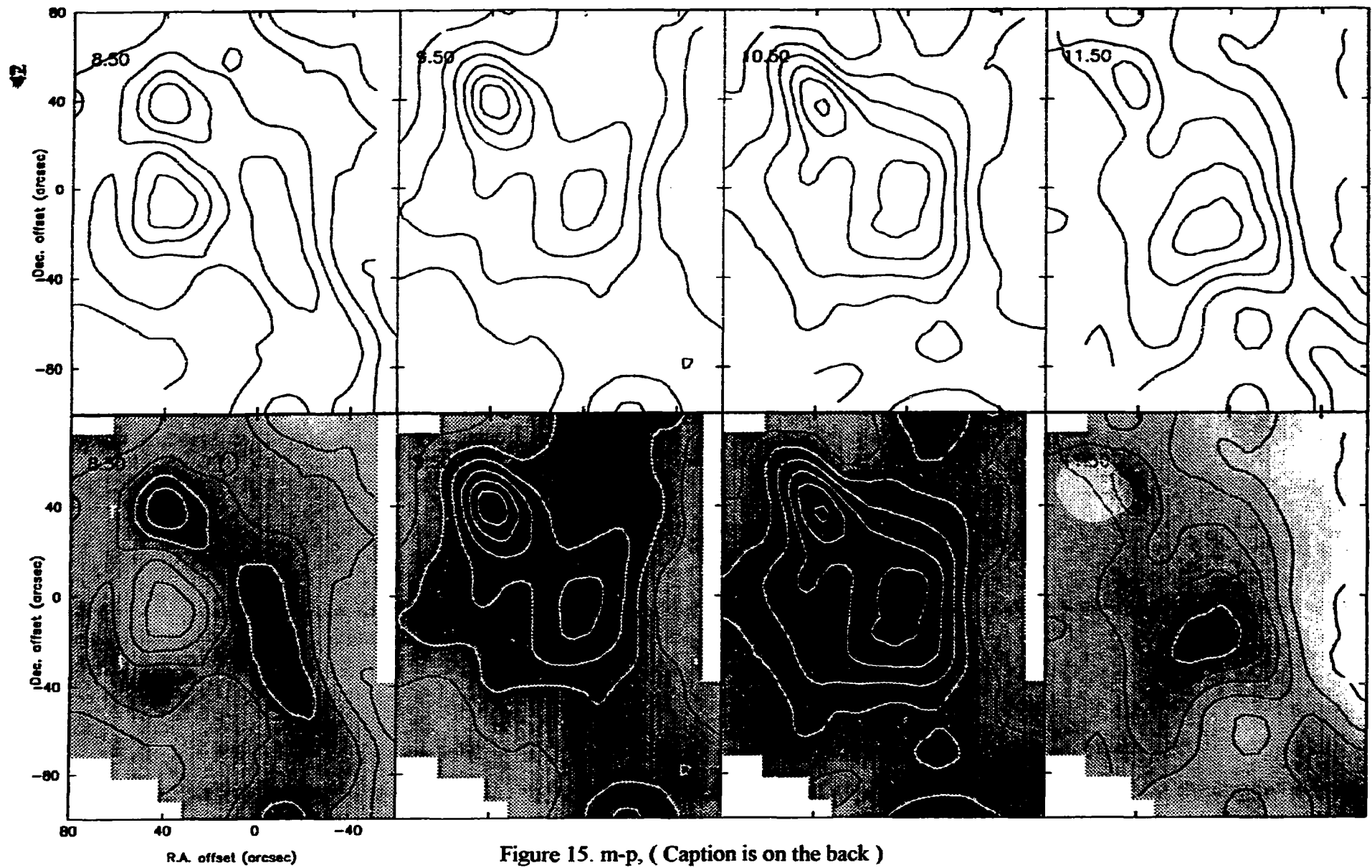


Figure 15. m-p, ( Caption is on the back )

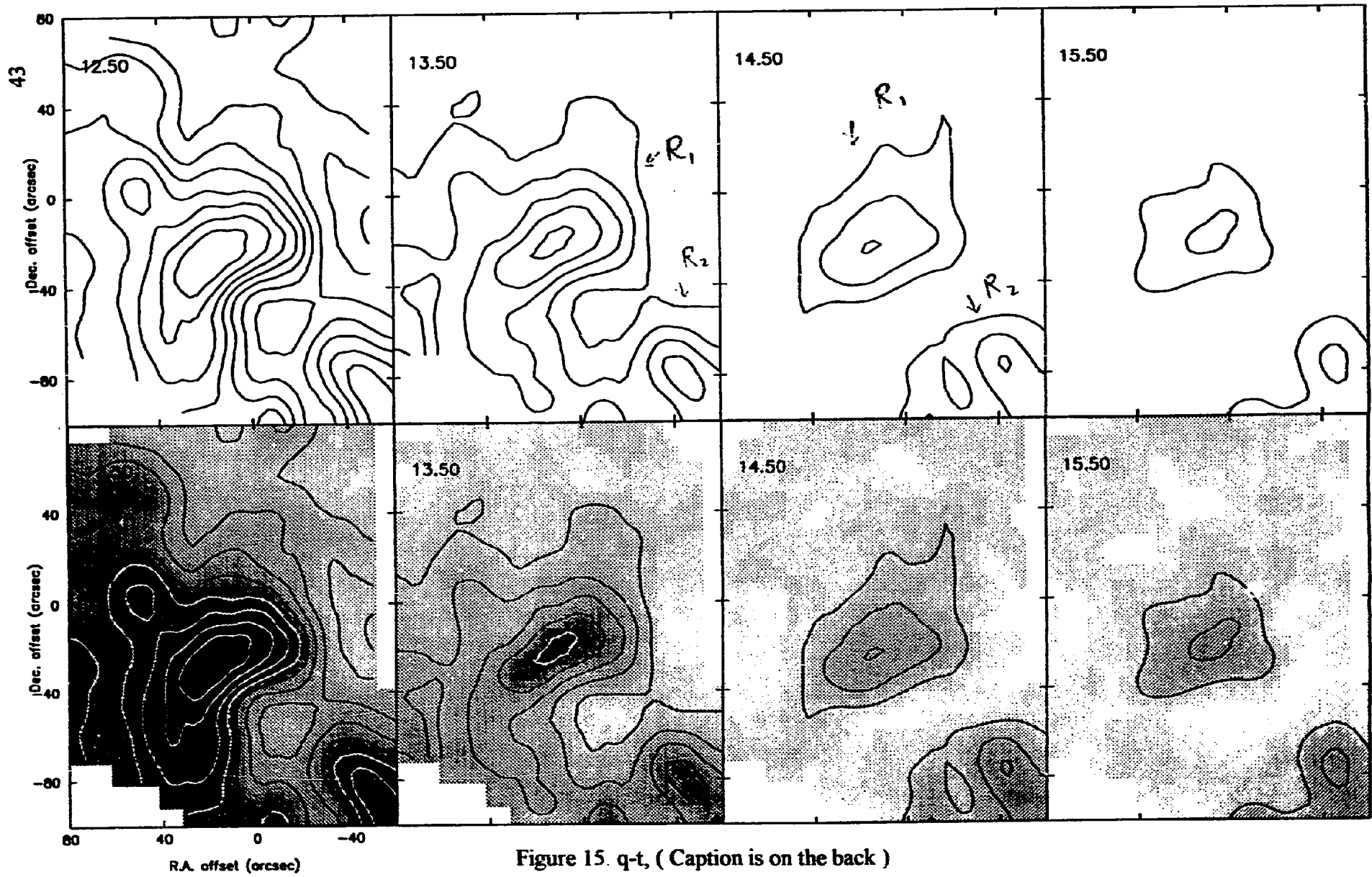


Figure 15. q-t, ( Caption is on the back )

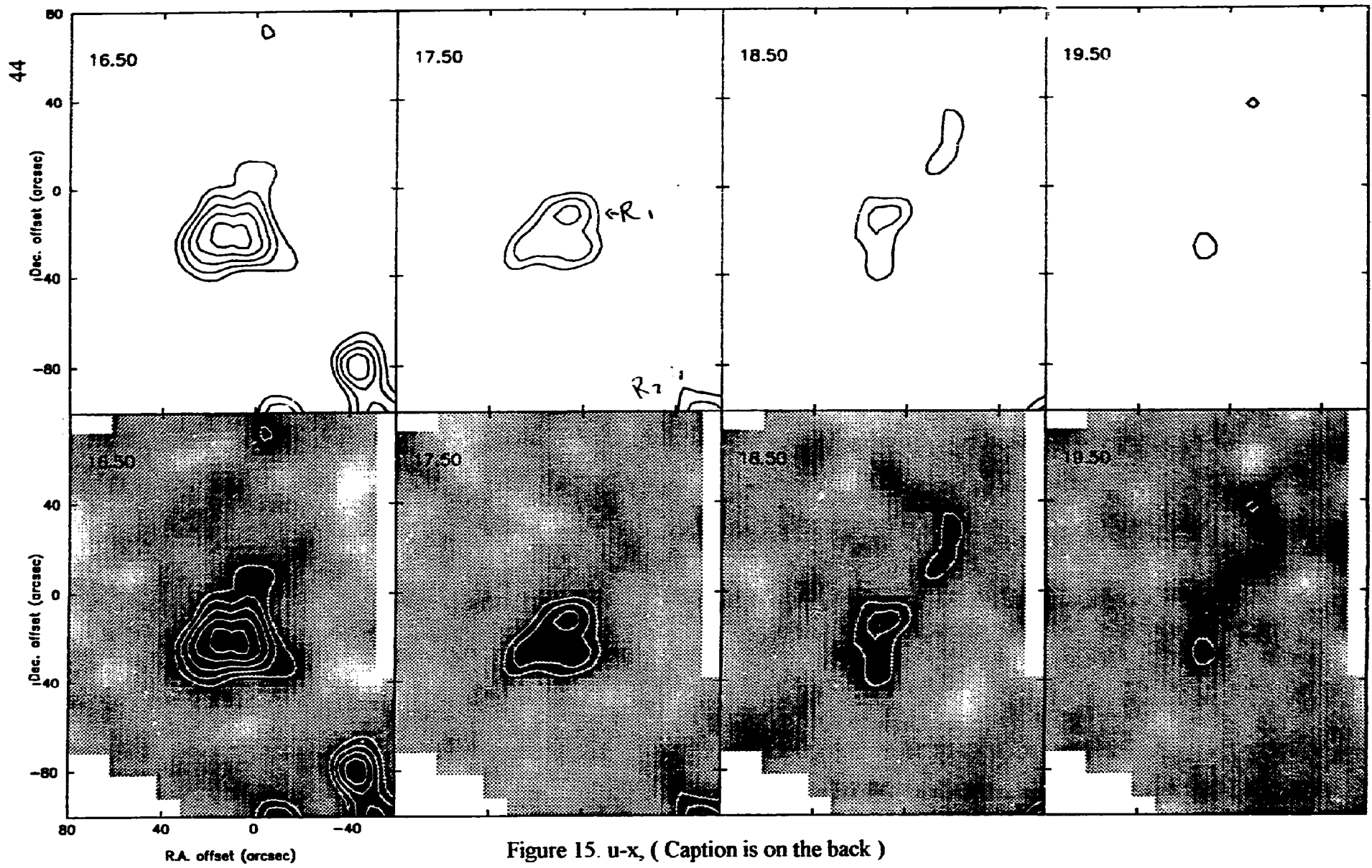


Figure 15. u-x, ( Caption is on the back )

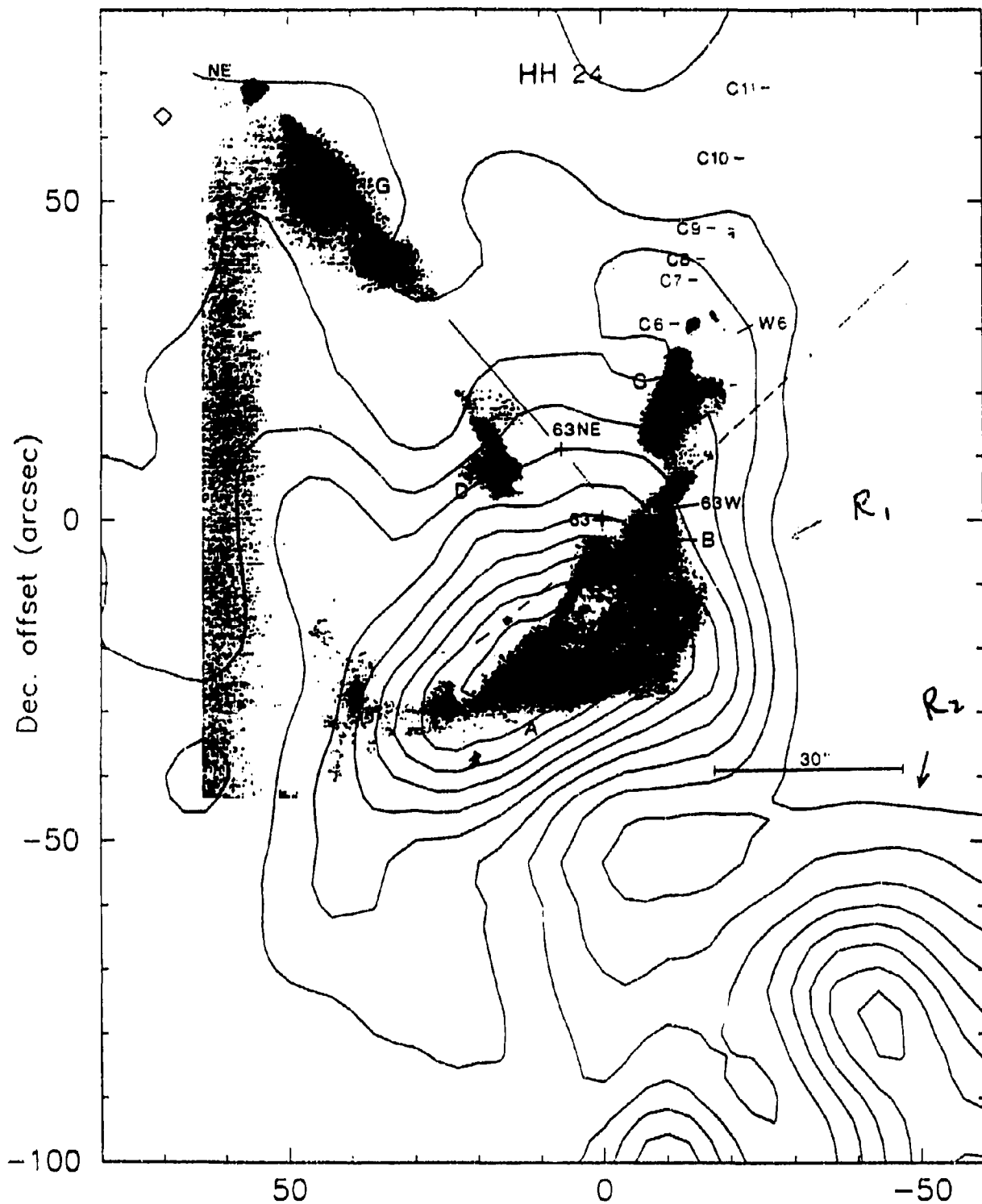


Figure 16. Map of the integrated  $^{12}\text{CO}$  J=3-2 redshifted emission overlaid on an [SII] CCD image observed by Mundt (1991). The redshifted emission is integrated from  $12 \text{ km s}^{-1}$  to  $20 \text{ km s}^{-1}$ , the lowest contour level is  $1 \text{ K-km s}^{-1}$  ( $1\sigma = 0.30 \text{ K-km s}^{-1}$ ) and the contour interval is  $1 \text{ K-km s}^{-1}$ .

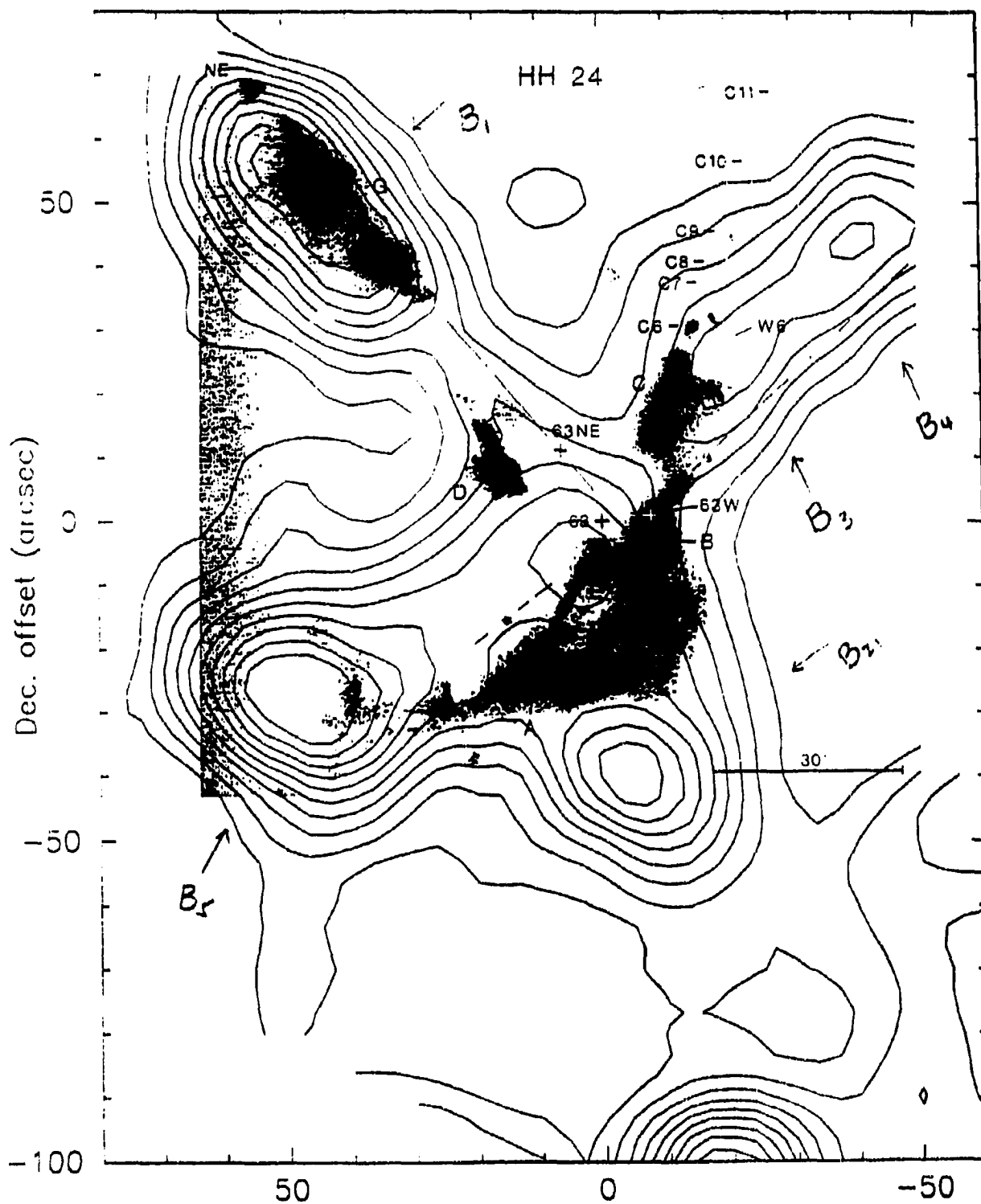


Figure 17. Map of the integrated  $^{12}\text{CO}$   $J=3-2$  blueshifted emission overlaid on an [SII] CCD image observed by Mundt (1991). The blueshifted emission is integrated from 2 to 5  $\text{km s}^{-1}$ , the lowest contour level is  $0.55 \text{ K-km s}^{-1}$  ( $1\sigma = 0.30 \text{ K-km s}^{-1}$ ) and the contour interval is  $0.30 \text{ K-km s}^{-1}$ .

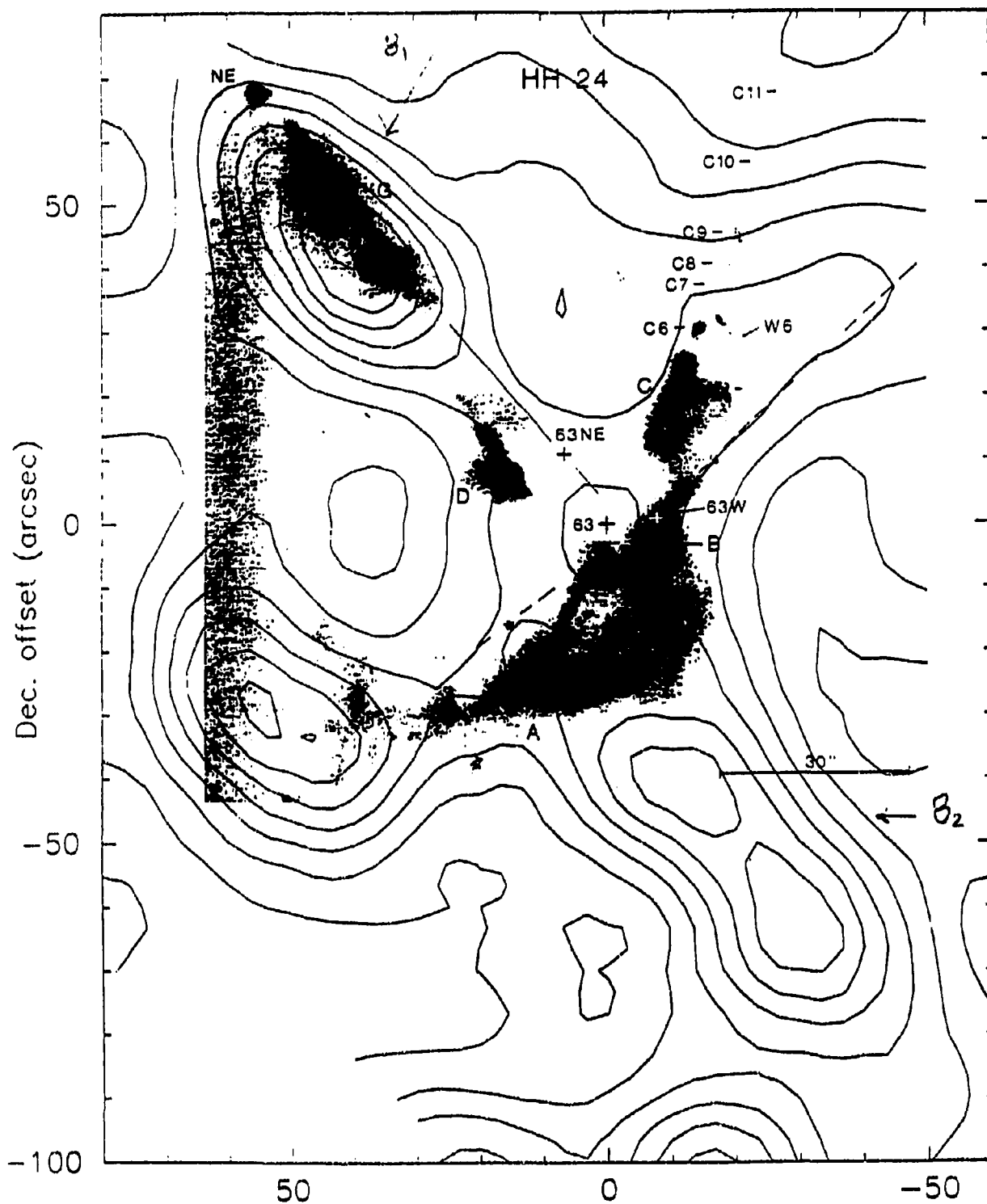


Figure 18. Map of the integrated  $^{12}\text{CO}$  J=3-2 blueshifted emission overlaid on an [SII] CCD image observed by Mundt (1991). The blueshifted emission is integrated from  $-4 \text{ km s}^{-1}$  to  $8 \text{ km s}^{-1}$ , the lowest contour level is  $2 \text{ K-km s}^{-1}$  ( $1\sigma = 0.30 \text{ K-km s}^{-1}$ ) and the contour interval is  $2 \text{ K-km s}^{-1}$ .

## IV. Physical Conditions of the Gas

The temperatures, density, mass, momentum and kinetic energy are important physical properties for understanding the nature of the molecular outflow phenomenon. Under the assumption that the isotopic abundance ratio of  $^{12}\text{CO}/^{13}\text{CO}$  is known and molecules are in a local thermodynamic equilibrium (LTE) with their surroundings, and using radiative transport of a line at frequency  $\nu$  in a plane-parallel cloud and radio astrophysics theory, all these parameters can be determined by observations of  $^{12}\text{CO}$  and  $^{13}\text{CO}$  emission from at least two rotational states. In this section, we describe how to derive these physical parameters from the spectral line observations.

### 1. Optical Depth

The optical depth of  $^{12}\text{CO}$  can be determined from the intensity ratio of  $^{12}\text{CO}/^{13}\text{CO}$  from the same transition. Because the frequencies for the same transition of  $^{12}\text{CO}$  and  $^{13}\text{CO}$  are very close, we assume that the telescope has the same beam size and efficiency for these lines. In our case, these lines are  $^{12}\text{CO}$  J=2-1 and  $^{13}\text{CO}$  J=2-1. With the additional assumptions that both isotopic species have the same excitation temperature and the isotopic abundance ratio (i.e.,  $X=N_{12}/N_{13}$ ) is known, we have

$$\frac{T_A^*(^{12}\text{CO})}{T_A^*(^{13}\text{CO})} = \frac{1 - e^{-\tau^{12}}}{1 - e^{-\tau^{12}/X}} \quad (1)$$

where  $T_A^*$  are the antenna temperatures the  $\tau^{12}$  is the optical depth of  $^{12}\text{CO } J=2-1$ . There is a limitation on the reliability with this method if the molecular line source is optically thick ( i.e.,  $1 \ll \tau^{13}$  ) since the antenna temperatures becomes insensitive to  $\tau^{13}$  in this situation. The  $^{13}\text{CO}$  optical depths is typically 0.01-0.06 ( Lada 1985 ) for most outflows, indicating that equation (1) provides a reliable way to determine the optical depth for most molecular outflows.

Figure 19 presents the  $^{12}\text{CO}/^{13}\text{CO}$  intensity ratio as a function of velocity over the entire velocity in which  $^{13}\text{CO}$  emission was detected at the 6 selected positions. At the line center, the  $^{12}\text{CO}/^{13}\text{CO}$  ratio of about 1.0, which indicates that the quiescent molecule gas in this region is quite optically thick. Assuming  $X=60$  ( Langer and Penzias, 1990 ), the optical depth of  $^{12}\text{CO}$  inner wings in this region is estimated to be  $2 < \tau < 6$ . The optical depth is not particularly sensitive to the choice of  $X$  when  $\tau^{12} = X\tau^{13} > 2$  ( Lada 1985 ). Our results are consistent with the results of SE82 that showed  $1 < \tau < 10$  with the assumption of a terrestrial isotopic ratio ( 89 ). As can be seen in figure 19, in most cases, the  $^{12}\text{CO}/^{13}\text{CO}$  intensity ratio increases away from the line center, which implies the optical depth decreases with increasing velocity. This suggests that the  $^{12}\text{CO } J=2-1$  optical depth in the outer wing is less than 1. We therefore assumed that the outer wings were optically thin.

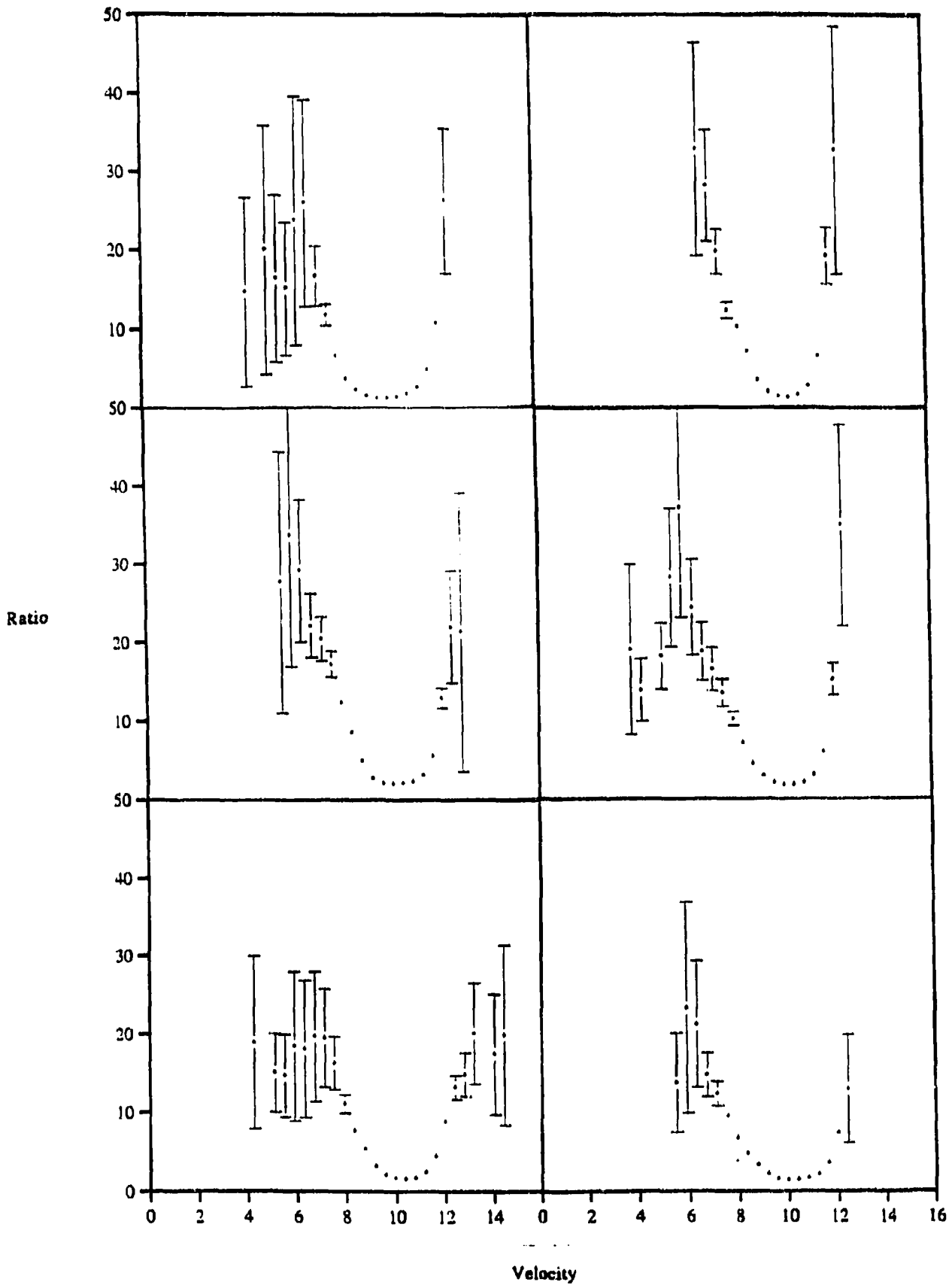


Figure 19. The  $^{12}\text{CO}/^{13}\text{CO}$  intensity ratio as a function of velocity over the entire velocity in which  $^{13}\text{CO}$  emission was detected at the 6 selected positions. The  $^{12}\text{CO}/^{13}\text{CO}$  intensity ratio increase away from the line center implies the optical depth are decrease at greater velocity.

Because of insufficient observing time, no  $^{13}\text{CO}$  J=3-2 spectra were obtained in our observations. Therefore we are unable to estimate the opacity of  $^{12}\text{CO}$  J=3-2 directly from observations. Instead we used a different method to estimate the optical depth of  $^{12}\text{CO}$  J=3-2 ( see below ).

## 2. Excitation Temperature

### a). Inner Wing

The excitation temperature  $T_{\text{ex}}$  can be estimated once the optical depth ( $\tau$ ) and the beam filling factor ( $f$ ) are known, using

$$\frac{T_A^*}{\eta_{\text{mb}} f} = (1 - e^{-\tau}) \frac{h\nu \kappa}{e^{h\nu/kT_{\text{ex}}} - 1} \quad (2)$$

The optical depth for  $^{12}\text{CO}$  J=2-1 can be estimated as described above. However, the beam filling factor is not known a priori. The assumption of a filling factor of unity may cause an underestimated excitation temperature and corresponding abundance ( see below ), if the actual distribution of molecular outflow is clumpy in nature. To avoid the problem caused by the beam filling factor, an alternative procedure would be used to determine the

excitation temperature from the ratio of the optical depth for the same isotope assuming LTE ( e.g. Snell et al. 1984 ),

$$\frac{\tau_{32}}{\tau_{21}} = \left(\frac{3}{2}\right) \left( \frac{1 - e^{-h\nu_{32}/kT_{ex}}}{e^{-h\nu_{21}/kT_{ex}} - 1} \right) \quad , \quad (3)$$

where  $T_{ex}$  is the common excitation temperature for the two transitions ( e.g. J=3-2 and J=2-1 ). Another attractive feature of this method, as indicated by Lada ( 1985 ), is that the determination of  $T_{ex}$  is not very sensitive to the details of absolute instrumental calibration since the individual opacity estimates are independent of antenna efficiencies. However, Choi et al. ( 1993 ) pointed out that if the outflows are clumpy, they may have unresolved multiple components with different optical depths. ( Though the difference of the optical depth is very difficult to assess, however if real,) The presence of multiple components may cause a serious underestimate of the excitation temperature, especially when the multiple components difference in optical depth by a factor of 2-3 or more.

Considering the uncertainties described above and mainly because of the lack of data for the  $^{13}\text{CO}$  J=3-2 in our observations, equation (2) was used to estimate the lower limit of excitation temperature with the assumption that the beam filling factor  $f=1$ . The results of average  $T_{ex}$  for both red and blue wings are summarized in table III. The average  $T_{ex}$  and  $\tau$  were calculated by taking a straight average over inner and outer range, separately.

b). Outer wing

The fact that  $^{13}\text{CO}$  J=2-1 is not detectable in the outer wings indicates that the optical depths for both  $^{12}\text{CO}$  J=2-1 and  $^{12}\text{CO}$  J=3-2 are optical thin. Thus in the case of the outer wings, the excitation temperature can be determined from the ratio of radiation temperatures with the assumption that the excitation temperature is the same in both transitions,

$$\frac{T_{R(32)}}{T_{R(21)}} = \frac{9}{4} e^{(-16.59 \cdot T_{ex})} \quad , \quad (4)$$

where the radiation temperature  $T_R = \frac{T_A^*}{\eta_{mb} f}$

Figure 20a presents the theoretical ratio of  $T_{R(32)} / T_{R(21)}$  as a function of  $T_{ex}$ . As can be seen in this figure, the ratio has an upper limit of 2.25 when  $T_{ex} \rightarrow \infty$ , and a small error in the ratio may cause a big uncertainty in  $T_{ex}$  at high temperatures ( $T_{ex} \geq 100\text{K}$ , corresponding to  $T_{R(32)} / T_{R(21)} \geq 1.9$ ). It should be emphasized that equation (4) can be only used in the optically thin situation. Figure 20b shows that, for the optically thick emission lines, the ratio of  $T_{R(32)} / T_{R(21)}$  is quite insensitive to  $T_{ex}$  and  $\tau$ . For the optically thin emission lines, the only limitation in this method is the problem caused by the

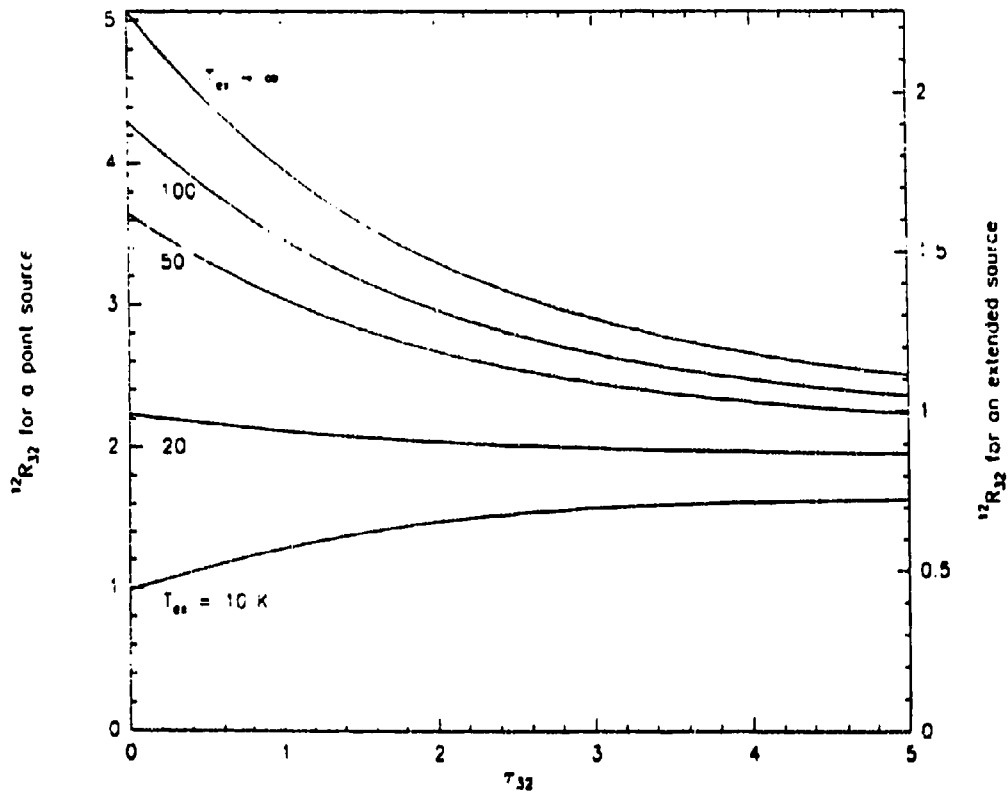
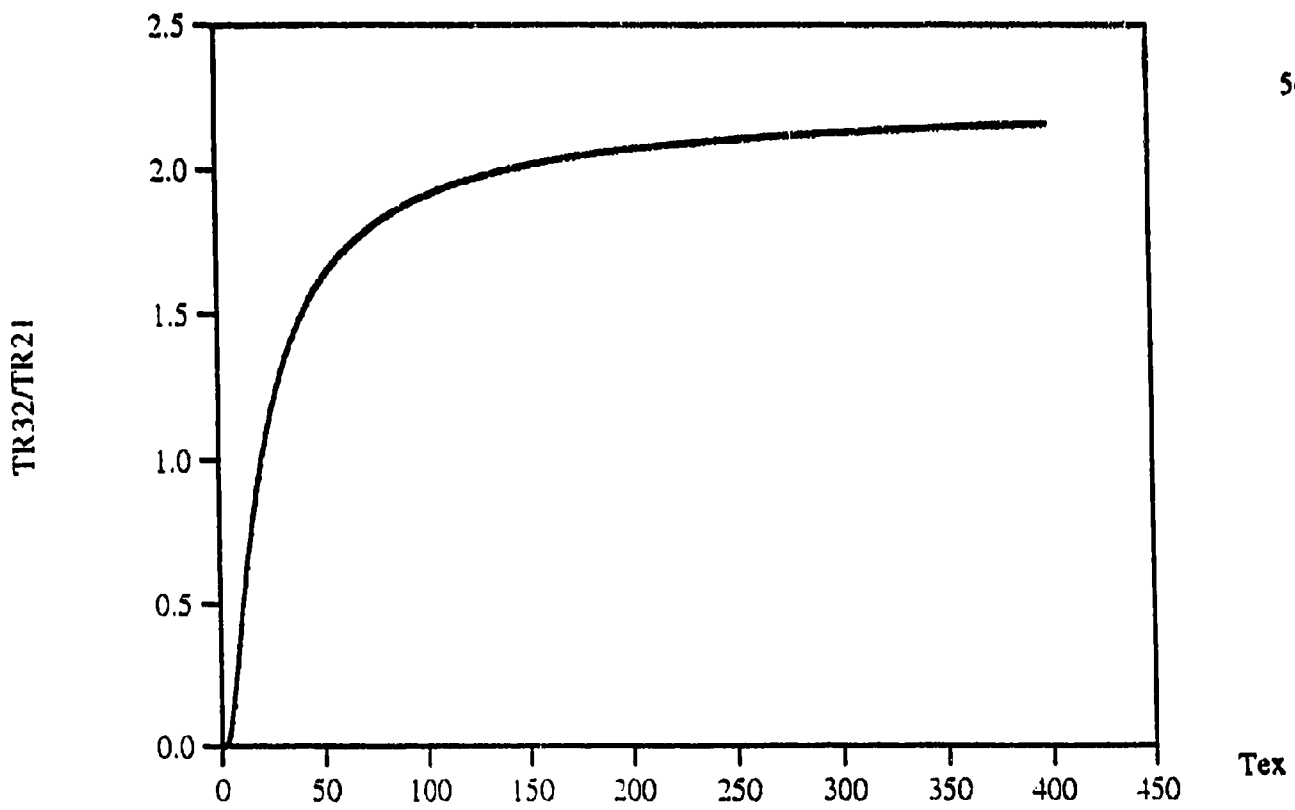


Figure 20 a). The theoretical ratio of  $TR_{32}/TR_{(32)}$  vs.  $T_{ex}$ . The ratio has an upper limit of 2.25 when  $T_{ex} \rightarrow \infty$ , and a small error in the ratio may cause a big uncertainty in  $T_{ex}$  at high temperatures ( $T_{ex} \geq 100$  K, corresponding to  $TR_{32}/TR_{(32)} \geq 1.9$ ). b). The ratio of  $TR(32)/TR(21)$  as a function of  $T_{ex}$  and optical depth  $\tau$  (adapted from Choi et al. 1993).

unknown filling factor. However, by assuming a point-like source located at the center both beams ( i.e.  $f_{21}/f_{32}=(2/3)^2$  because  $(2/3)^2$  is the lower limit to  $f_{21}/f_{32}$  ), a lower limit to  $T_{R(32)}/T_{R(21)}$  is estimated, thus a lower limit to  $T_{ex}$  can be calculated. Alternatively, by assuming an extended source ( i.e.  $f_{21}/f_{32}=1$  ), an upper limit of  $T_{ex}$  can be estimated.

The main beam temperature is defined as  $T_{MB}=\frac{T_A^*}{\eta_{mb}f}$  ( i.e the radiation temperature without any correction for the filling factors ). Figure 21 shows the main beam temperature ratio of  $T_{mb(32)}/T_{mb(21)}$  as a function of velocity at the 6 selected positions in our observations. Table III shows both the lower and upper limits of  $T_{ex}$  calculated in the outer wings at the 6 positions. As can be seen in Figure 21, the dispersion of the intensity ratio of  $^{12}\text{CO J=3-2}$  and  $^{12}\text{CO J=2-1}$  is too large to accurately estimate  $T_{ex}$  at each velocity point. To reduce the statistical uncertainty, the integrated intensity is used in equation (4) to calculate the velocity-averaged excitation temperatures. It can be seen that in most cases the lower limit temperatures in the outer wings are in good agreement with the results of the inner wings. Therefore the lower limit temperatures are used in the following calculations. The estimate of  $T_{ex}$  by Snell and Edwards ( SE82 ) is 10K, which is reasonably close to our results. The velocity-averaged excitation temperatures are weighted by those in the relatively low velocities.

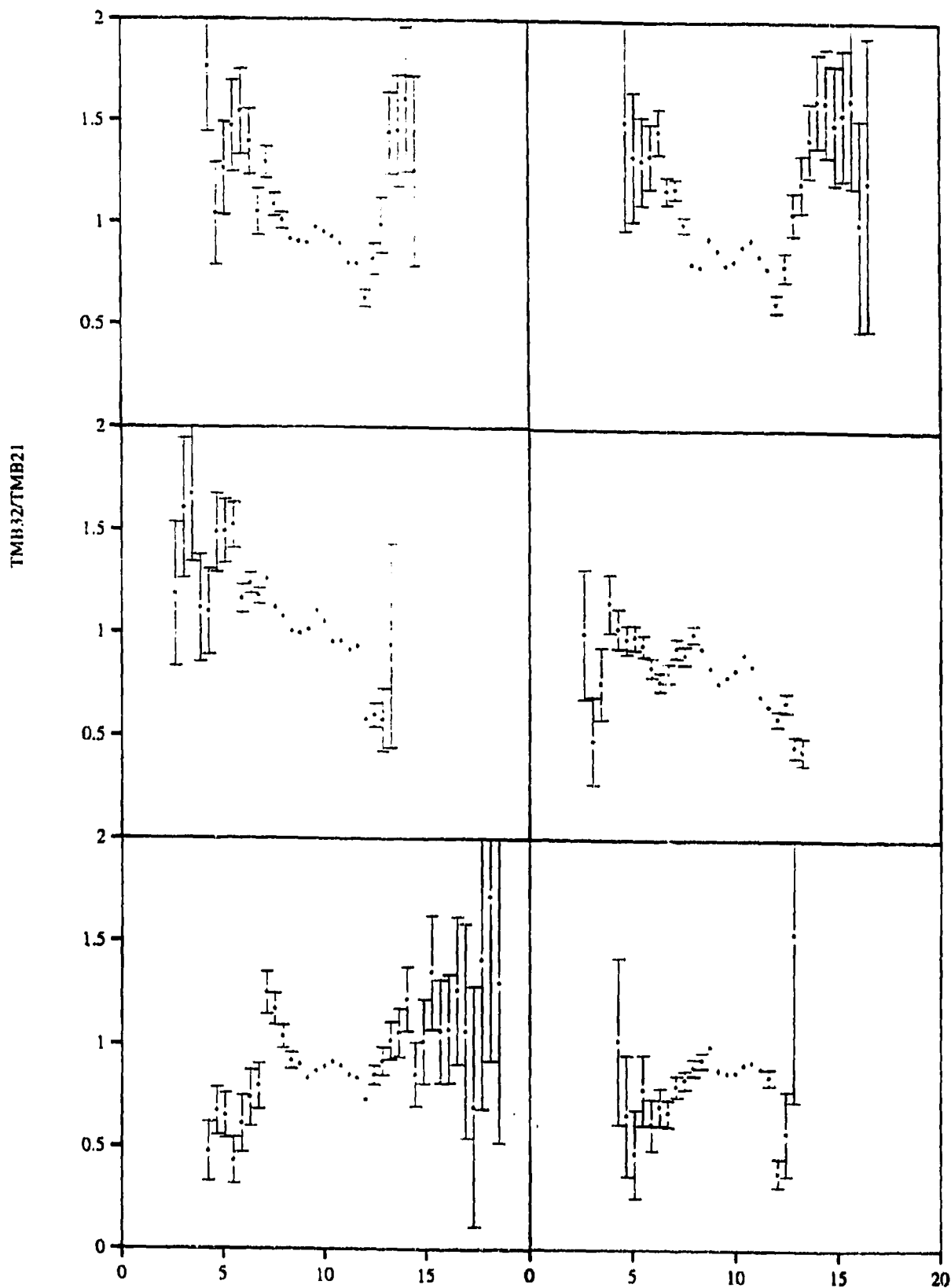


Figure 21. The main beam temperature ratio of  $Tmb(32)/Tmb(21)$  as a function of velocity at the 6 selected positions.

Table III  
Excitation Temperature at the 6 selected Positions

Positions	Wing	$\tau$	$T_{\text{ex}}$ (K)	
			upper limits	lower limits
(0,0)	Outer blue	.....	42.38	13.80
	Inner blue	4.19	.....	10.41
	Inner red	3.93	.....	14.24
	Outer red	.....	37.90	13.27
(-40,-70)	Outer blue	.....	28.52	11.91
	Inner blue	3.48	.....	16.66
	Inner red	2.22	.....	13.23
	Outer red	.....	30.06	12.17
(40,40)	Outer blue	.....	54.87	14.90
	Inner blue	3.39	.....	18.36
	Inner red	3.38	.....	11.05
	Outer red	.....	13.23	8.03
(50,-30)	Outer blue	.....	16.37	9.09
	Inner blue	3.90	.....	13.74
	Inner red	2.64	.....	15.48
	Outer red	.....	8.09	5.80
(10,-20)	Outer blue	.....	11.90	7.52
	Inner blue	4.29	.....	10.11
	Inner red	4.21	.....	11.71
	Outer red	.....	22.54	10.73
(-10,20)	Outer blue	.....	17.40	9.40
	Inner blue	5.87	.....	13.74
	Inner red	4.31	.....	8.49
	Outer red	.....	22.25	10.66

### 3. Column Density

The  $^{12}\text{CO}$  column density  $N_i(^{12}\text{CO})$  for each channel  $i$  in the optically thin limit ( the outer wings ) can be determined by assuming that the level populations are in LTE at a temperature  $T_{\text{ex}}$ ,

$$N_i(^{12}\text{CO}) (\text{cm}^{-2}) = 4.64 \times 10^{12} T_{\text{ex}} e^{-33.18/T_{\text{ex}}} \times T_{R32} \Delta V (\text{km s}^{-1}) \quad , \quad (5)$$

where  $\Delta V$  is the channel width in  $\text{km s}^{-1}$ .  $T_R$  is the corresponding radiation temperature at the channel.

The estimate of  $^{12}\text{CO}$  column density  $N_i(^{12}\text{CO})$  for each channel  $i$  in the inner wings based on the optically thin approximation must be corrected for optical depth effects. The correction is made by multiplying equation (5) by a factor  $\tau/(1-e^{-\tau})$

$$N_i(^{12}\text{CO}) (\text{cm}^{-2}) = 4.64 \times 10^{12} T_{\text{ex}} e^{-33.18/T_{\text{ex}}} \times T_{R32} \Delta V (\text{km s}^{-1}) \tau/(1-e^{-\tau}), \quad (6)$$

where  $\tau$  is the mean optical depth of  $^{12}\text{CO}$   $J=3-2$  which is calculated by using equation (3) under the assumption that the two transitions (  $J=2-1$  and  $J=3-2$  ) have the same  $T_{\text{ex}}$  which are derived through equation (2).

By assuming a ratio of molecular hydrogen column density to  $^{12}\text{CO}$  column density of  $N(\text{H}_2)/N(^{12}\text{CO}) \approx 1 \times 10^4$ , the total molecule hydrogen column density at each channel can be estimated. Since determinations of mean optical depth and excitation temperature were made at only 6 positions, we must assume that the mean optical depth and excitation temperature at the other positions are equal to those at the closest of the 6 positions. This assumption is somewhat arbitrary, because the distribution of molecular gas in this region is very complex. However calculations show that the column densities are not very sensitive to the choice of  $T_{\text{ex}}$  ( especially for lower rotational levels ). The factor  $T_{\text{ex}} e^{33.18/T_{\text{ex}}}$  varies by only a factor of 3 over the range 10-40 K. But in the optically thick wings, an error in optical depth combined with those in  $T_{\text{ex}}$  may cause a larger error in  $N(^{12}\text{CO})$ . If the level population of molecules does not correspond to local thermodynamic equilibrium, the assumption of LTE may lead a overestimate of column density.

#### 4. Mass, Momentum and Kinetic Energy

Based on the calculation of the column density of  $\text{H}_2$ ,  $N_i(\text{H}_2)$ , the mass for each channel velocity interval can be determined by

$$M_i(\text{H}_2) = N_i(\text{H}_2) \times m(\text{H}_2) \times A, \quad (7)$$

where  $m(H_2)$  is the mass of a molecule hydrogen and  $A$  is the projected area subtended by emission in that channel. The total gas mass per channel can be obtained by taking into account the fractional helium abundance of 10% by number:

$$M_i = 1.4 M_i(H_2) \quad (8)$$

The mass, momentum and kinetic energy at each position within each wing interval ( see table IV ) can then be determined from

$$M = \sum_i M_i \quad (9)$$

$$P = \sum_i M_i |V_i - V_o| \quad (10)$$

$$E_k = \sum_i \frac{1}{2} M_i (V_i - V_o)^2 \quad (11)$$

where  $V_o = 10.2$  (  $\text{km s}^{-1}$  ) is the velocity of the ambient gas ( see part III ). Summing over all locations, the total mass , momentum and kinetic energy for the red and blue wings can be determined. The mass, momentum and kinetic energy for each clump is also calculated by using the same method. The calculated values are shown in table III. Errors in the mass estimates are already discussed in the previous parts. Unlike the mass, the momentum and kinetic energy are dependent on the orientation of the outflows by factors of  $1/\sin\theta$  and  $1/\sin^2\theta$ , respectively, since only the radial velocity is measured, where  $\theta$  is the

angle between the flow axis and the plane of the sky. Because no attempt has been made to account for the projection effects, the momentum and kinetic energies are lower limits.

Table IV  
Physical Parameters of Outflow

	Velocity range ( km s <sup>-1</sup> )	Mass ( M <sub>⊙</sub> )	Momentum(P) ( M <sub>⊙</sub> km s <sup>-1</sup> )	Kinetic Energy (E <sub>k</sub> ) ( 10 <sup>44</sup> ergs )
Total Outer blue	-5.02 ~ 5.02	0.0435	0.3302	0.2861
Total Inner blue	5.29 ~ 8.28	1.1015	2.9306	0.9114
Total Inner red	12.08 ~ 12.62	0.1870	0.4209	0.0987
Total Outer red	12.89 ~ 20.22	0.0479	0.2227	0.1245
Lobe B1	-5.02 ~ 5.02	0.0067	0.0529	0.0470
	5.29 ~ 8.28	0.150 <sup>o</sup>	0.4349	0.1336
Lobe B3+B4	-5.02 ~ 5.02	0.0063	0.0511	0.0464
	5.29 ~ 8.28	0.2557	0.7426	0.2297
Lobe B2	-5.02 ~ 5.02	0.0111	0.0749	0.0591
	5.29 ~ 8.28	0.1324	0.3553	0.1000
Lobe B5	-5.02 ~ 5.02	0.0059	0.0462	0.0400
	5.29 ~ 8.28	0.1685	0.5219	0.1790
Lobe R1	12.08 ~ 12.62	0.0887	0.2168	0.0560
	12.89 ~ 20.22	0.0195	0.0924	0.0522

## 5. Dynamical age, Momentum Flux and Mechanical luminosity

The dynamical time scale  $t_{dyn}$  for the formation of the outflow can be estimated by

$$t_{dyn} = R / \langle V \rangle, \quad (12)$$

where  $\langle V \rangle$  is the mean velocity of the gas weighted by mass,  $\langle R \rangle$  is the mean physical size of the outflow lobe.

The mean velocity for the two lobes ( B1 and B3+B4 ) can be determined from the ratio of their total momentum to their total mass. The resulting values are  $\langle V \rangle \approx 3.10 \text{ km s}^{-1}$  and  $\langle V \rangle \approx 3.03 \text{ km s}^{-1}$ , respectively. This indicates that the bulk of the mass of the molecular outflows is moving with a velocity much smaller than the maximum observed outflow velocity (  $\sim 15 \text{ km s}^{-1}$  with respect to the ambient gas velocity at  $V_{LSR} = 10.2 \text{ km s}^{-1}$  ). A comparison of velocity in the HH24 region with typical bipolar outflows indicates that the molecular gas studied here covers a considerably small velocity range. The mean physical sizes for the two lobes are crudely determined by measuring the distance of their emission peaks to the driving sources. The results are given in Table V.

Similar to the momentum and kinetic energy, the dynamical time is also dependent on the orientation of the outflows. Since  $\langle V \rangle$  is the mean radial velocity and  $\langle R \rangle$  is the projected length, the correction required for the dynamical time is given by a factor of  $\tan$

$\theta$ . The correction for the inclination of the outflow tends to shorten the dynamical time when the  $\theta$  is less than  $45^\circ$ . Combining the estimate of dynamical time with the estimates of momentum and energy in the molecular outflow, the momentum flux,  $F=MV/t_{\text{dyn}}$  and the mechanical luminosity,  $L_m=MV^2/2t_{\text{dyn}}$  can be determined. The results are presented in Table V.

Table V  
Characteristics of Outflows

	$\langle V \rangle$ ( $\text{km s}^{-1}$ )	$\langle R \rangle$ (pc)	$t_{\text{dyn}}$ ( $10^4$ yr)	Momentum(P) Flux ( $10^{-5} M_{\odot} \text{ yr}^{-1} \text{ km s}^{-1}$ )	$L_m$ ( $10^{-2} L_{\odot}$ )
Lobe B1	3.10	0.15	4.7	1.04	0.32
Lobe B3+B4	3.03	0.14	4.5	1.76	0.50

## **V. Discussion**

### **1. Morphology and General Properties of the Outflows**

We have estimated the mass, momentum, kinetic energy and the dynamical time of the molecular outflow using techniques similar to those employed by Snell et al. ( 1984 ). The results are in good agreement with typical values found for other bipolar outflows. A comparison of our results with the values calculated for HH24 by Snell and Edwards ( SE82 ) shows that those studied here are about 3 times less in mass, 4 times less in momentum and one order of magnitude less in kinetic energy. The discrepancy can be well explained by the small size of our mapping region. The mapped region is dominated by blueshifted emission. The mass and momentum of blueshifted gas are 5 times more than those of the redshifted gas. The imbalance in mass between blue and red components is similar to those found in S140 ( Snell et al. 1984 ) and GL2591 ( Mitchell et al. 1992 ). A similar but red dominant imbalance is found in sources NGC 2024 ( Richer et al. 1989 ), HH46-47 ( Chernin and Masson 1991 ), and W3 /IRS5 ( Mitchell et al. 1992 ). The mechanism responsible for such asymmetric outflows is not well understood. In the case of NGC2024, Richer et al. propose that the unipolar appearance might be due to the asymmetric environment of the star, arguing that the need for a balanced momentum suggests the initially symmetric flow. In the case of GL2591, blueshifted gas far exceeding red-shifted gas in mass is attributed to the lack of observations due to the foreground absorption ( Mitchell et al. 1992 ). In the case studied here, the asymmetry in mass and momentum may be due to the red-shifted velocity being too small to distinguish

from ambient molecular material, or may be due to the redshifted gas extending far beyond the mapped region.

The mapped region shows a rather complex morphology of  $^{12}\text{CO}$  emission. Our observations have identified 4 distinct elongated blue lobes aligned in two lines along NE-SW and NW-SE directions. The distribution of the blue-shifted emission could admit two alternative explanations. In the first interpretation, one might think the 4 blue lobes are not connected but separated outflows. This interpretation is unattractive because only 3 IR sources have been identified around the center of the 4 lobes and it is unlikely that 3 IR sources power 4 outflows in 4 directions. A more plausible explanation of the observed feature is that the 4 blueshifted components belong to two outflows which blend together at the place near the map center. One is traced by B1 and B2 in NE-SW direction ( hereafter referred to as EBL1 ). The other one is traced by B3, B4 and B5 in NW-SE direction ( hereafter referred to as EBL2 ). As mentioned earlier, one of the two distinct red lobes ( R1 ) may be the red-shifted counterpart of the lobe B1. Since B1 is spatially associated with HH24G jet which is powered by SSV63NE ( Mundt et al. 1991 ), we identify SSV63NE as the exciting source of EBL1 and R1. Two possible candidates for the driving source of EBL2 are SSV63 and SSV63W. Because they are spatially very close, it is not possible to tell which is responsible for EBL2. We assume that one or both of them could be responsible for driving the outflow EBL2.

To understand actual 6-dimensional dynamical structure from the observed 3-dimensional phase space is very difficult. It has been suggested by Cabrit and Bertout ( 1986, 1990 ) and Meyers-Rice and Lada ( 1991 ) that the orientation of the flow axis with respect to the line of sight plays a major role in the appearance of the flow. Figure 22, taken from Cabrit and Bertout ( 1986 ), illustrates this points. The elongated structure of EBL1 and EBL2 suggests that the orientations of the two blue lobes are approximately similar to the case 3 outflow class as defined by Cabrit and Bertout ( bottom left of Fig. 22 ). That is, the angle of inclination of the outflows in the HH24 region with respect to the plane of the sky is very small. However, the two outflows do not appear to be biconical in shape. Instead, they likely have a paraboloidal ( Fig. 23 ) or a approximate cylindrical overall structure. Such an outflow with a small inclination would have mixed red-shifted and blue-shifted emission on both sides of the center source and would not appear as bipolar but simply elongated. However the relative weakness of red-shifted emission in the outflows in our observation present a problem for this interpretation. A possible explanation is that the velocity at the redshifted gas is too small to distinguish from the ambient molecular material, and thus, the red-shifted outflow material is missed, rather than absent, in our observations. Another possible explanation is that the outflow exist in a very complex region of the star formation, and that the dynamical structure of the molecular outflow is complicated likewise.

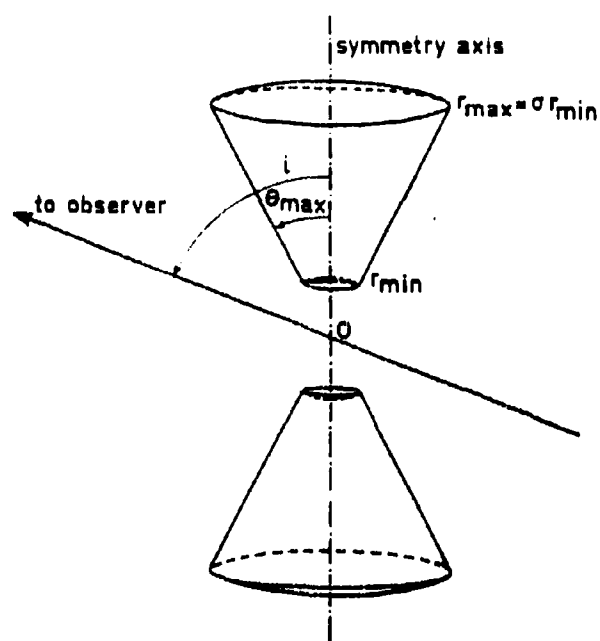
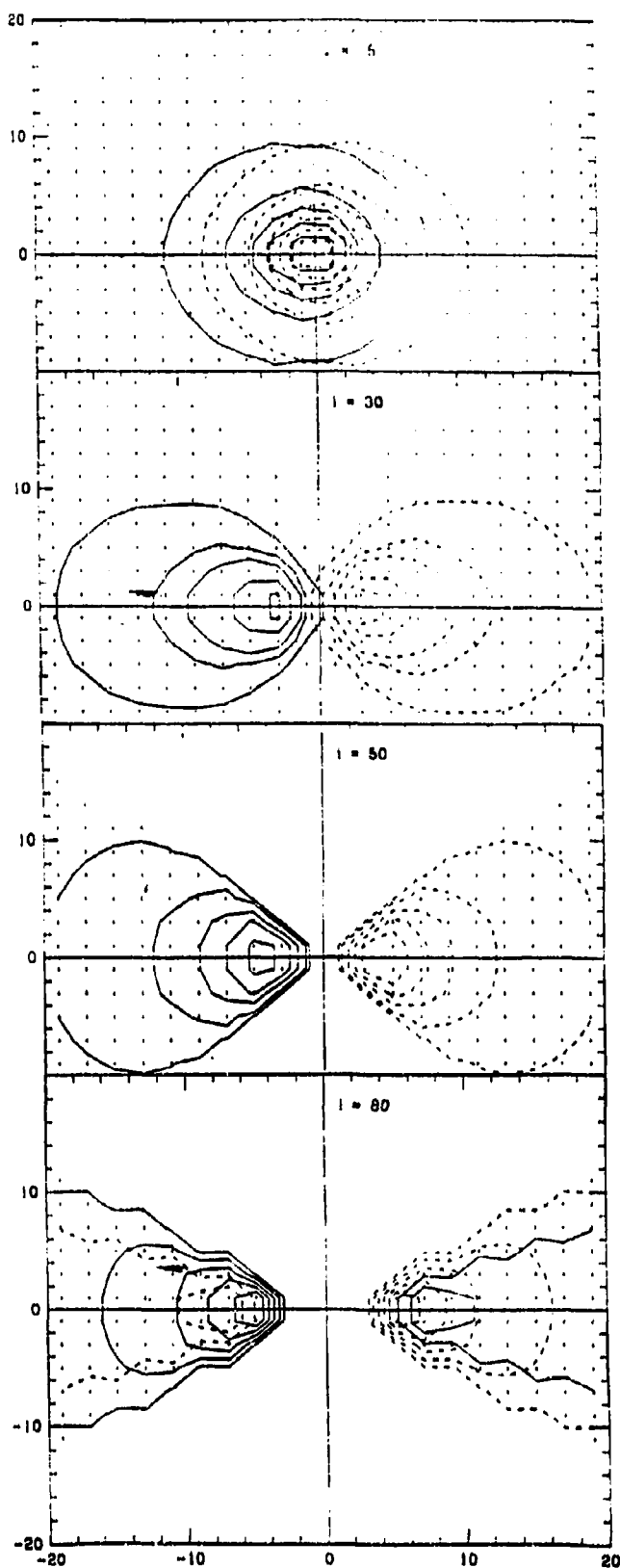


Figure 22. Models of a conical bipolar outflow with a 30° degree opening angle as seen from the source. The outflow is assumed to have two filled biconical flow lobes with the flow vectors parallel to the flow surface. The models are views from four different angles ( 5°, 30°, 50°, and 80° ). A nearly face-on flow ( top left ) shows poor collimation, while a flow whose axis lies close to the plan of the sky appears well collimated ( bottom left ) ( from Cabrit and Bertout 1986 ).

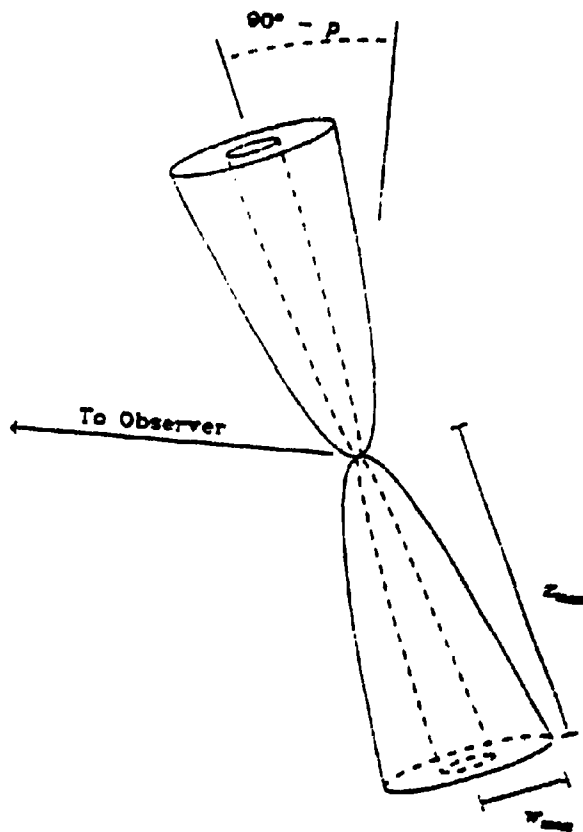


Figure 23. A schematic paraboloidal outflow model. Each outflow lobe is described by a thin paraboloidal shell ( from Meyers-Rice and Lada 1991 ).

## 2. Relationship to Optical Jets

The striking evidence for the correlation of the  $^{12}\text{CO}$  emission and the optical jet occurs around the HH24G jet and the HH24A working surface as can be seen in Figure 17, Figure 18 and Figure 16. The blue-shifted  $^{12}\text{CO}$  lobe B1 covers the full extent of the optically visible blue-shifted HH24G jet with the HH24G passing through its center. The spatial coincidence among the red-shifted  $^{12}\text{CO}$  peak R1,  $\text{H}_2$  emission,  $2.12\mu\text{m}$  emission source ( Zealey et al. 1992 ), and optical emission the HH24A suggests that the gas under the different excitation condition is highly mixed in this region, which has a scale size smaller than the spatial resolution. Although EBL2 covers the brightest part of optical jet HH24C and most part of the third optical jet traced by several faint knots, there are significant deviations from perfect symmetry in the alignment of the  $^{12}\text{CO}$  emission ( EBL2 ) and each of the two optical jets. EBL2 is rotated a few degrees with respect to the optical jet HH24C, while EBL2 and the faint optical jet are oriented parallel to each other with a significant spatial offset of a few arcseconds between their axes. A similar phenomenon was observed in NGC2071 where the shocked  $\text{H}_2$  is parallel to the molecular flow, but offset so that it lies along the southern edge of the flow ( Lane & Bally 1986 ). Because of the offsets, it is not clear which of the optical jets is related to EBL2 or if any of them is related at all.

One of the key questions to study the relationship of molecular outflows to optical jet is: does the optical jet have enough momentum to drive the molecular outflow? Mundt

et al. ( 1991 ) has shown that mass loss rates in the jet scale roughly with  $L_{\text{bol}}^{0.6}$ , where  $L_{\text{bol}}$  is the bolometric luminosity of the source. Based on the observation of HH24C, Mundt found that the mass loss rate of for HH24C is  $10^{-9} M_{\odot} \text{ yr}^{-1}$ . If the correlation between stellar luminosity and mass loss rate in the jet is applicable to HH24G and its driving source SSV63NE, we can get the mass loss rate for HH24G jet under the assumption that SSV63NE has the same luminosity as SSV63. If we use  $300 \text{ km s}^{-1}$  as a characteristic jet velocity, the momentum flux carried by the optical jet is  $3 \times 10^{-7} M_{\odot} \text{ yr}^{-1} \text{ km s}^{-1}$ . This is two orders of magnitude smaller than the value of  $1.04 \times 10^{-5} M_{\odot} \text{ yr}^{-1} \text{ km s}^{-1}$  calculated for the CO outflow and is incapable of driving the molecular outflow. If, however, the optical jet is only partially ionized, the momentum flux for the optical jet will increase to  $10^{-6} M_{\odot} \text{ yr}^{-1} \text{ km s}^{-1}$  by using a correction for an ionization of 10% ( Raga 1991 ). The result is still too small. However , as stressed by Raga ( 1991, 1993 ), the determination of momentum rate for optical jet is strongly model-dependent. A different consideration based on no correction for compression at a shock could yield estimates for the mass loss rate one to three orders magnitude larger than those given by Mundt et al. 1987 ( Raga 1991 ). In this case, the mass loss rate for the jet is very close to the values of that of CO outflow and are comparable with the requirement for driving the molecular outflow.

## VI. Conclusion

Our new high angular resolution observations reveal a complex morphology and kinematics of CO molecular emission associated with HH24 complex. Our interpretation of these data is that the bulk of blueshifted gas arise in two outflows. The scarcity of redshifted counterpart of the flows remains a fundamental problem that needs to be addressed in future observations. In the northeast of the map the CO blueshifted flow aligns well with the HH24G blue jet. Near the map center redshifted CO is coincident with the shocked H<sub>2</sub> source and the HH24A. The spatial coincidence indicate CO outflows and the optical outflow may be physically associated phenomena. The momentum flux in the CO outflow is about one order of magnitude larger than that derived from the optical jet after applying corrections for the partial ionization and this suggests that the ionized jet might be incapable of driving the molecular outflow in this case. However, due to the uncertainties in determination of momentum flux for both optical jet and molecular outflow, this conclusion should be regarded only as most tentative.

## Reference

- Bachiller, R. and Cernicharo, J., 1990, *A&A*, **239**, 276.
- Bachiller, R. and Cernicharo, J., 1991, *A&A*, **251**, 639.
- Bally, J., and Lada, C. J., 1983, *Ap.J*, **265**, 824.
- Bally, J. and Lane, A.P., 1991, in : *The Physics of Star Formation and Early Stellar Evolution*. Lada, C.J., Kylafis, N.D. (eds.) Kluwer, Dordrecht. P. 471.
- Blandford, R. D., and Rees, M.J., 1974, *M.N.R.A.S.*, **169**, 395.
- Cabrit, S. and Bertout, C., 1986, *Ap.J*, **307**, 313.
- Cabrit, S. and Bertout, C., 1990, *Ap.J*, **348**, 530.
- Chernin, L. M., and Masson, C. R., 1991, *Ap.J*, **382**, L93.
- Chernin, L. M., and Masson, C. R., 1994, *Ap.J*, **426**, 204.
- Cohen, M., and Schwartz, R. D., 1983, *Ap.J*, **265**, 877.
- Cohen, M., Harvey, P. M., Schwartz, R. D., and Wilking, B. A., 1984, *Ap.J*, **278**, 671.
- Dopita, M.A., Schwartz, R. D., and Evans, I., 1982, *Ap.J*, **263**, L73.
- Draine, B. T., 1983, *Ap.J*, **276**, L9.
- Dyson, J. E., 1987, in: *Circumstellar Matter*, eds. Appenzeller, I. & Jordan, C. (Reidel: Dordrecht, Netherlands), P.159.
- Edwards, S., and Snell, R., 1984, *Ap.J*, **281**, 237.
- Edwards, S., Ray, T., and Mundt, R., 1991, in. *Protostars & Planets III*. University of Arizona Press, Tucson. Levy, E. H., and Lunine, J. (eds.)
- Fridlund, C. V. M., Sandqvist, A., Nordh, H. L., and Olofsson, G., 1989, *A&A*, **213**, 310.
- Fukui, Y., Iwata, M., Mizuno, A., Bally, J., Lane, A.P., 1991, in: *Protostars & Planets III*. University of Arizona Press, Tucson. Levy, E. H., and Lunine, J. (eds.), P. 603.
- Gibb, A.G., and Heaton, B.D., 1993, *A&A*, **276**, 511.
- Hartigan, P., Raymond, J., and Meaburn, J., 1990, *Ap.J*, **362**, 624.

- Hartigan, P., Raymond, J., and Meaburn, J., 1990, *Ap.J*, **362**, 624.
- Haschick, A. D., Moran, J. M., Rodriguez, L. F., and Ho, P., 1983, *Ap.J*, **265**, 281.
- Jones, B. F., Cohen, M., Wehinger, P. A., and Gehren, T., 1987, *A.J*, **94**, 1260
- Kwan, J., and Scoville, N.Z., 1976, *Ap.J*( letters), **210**, L39.
- Koo, B. C., 1990, *Ap.J*, **337**, 318.
- Lada, E. A., Bally, J., and Stark, A. A., 1991, *Ap.J*, **368**, 432.
- Lada, E. A., Depoy, D. L., Evans, N. J., and Gatley I., 1991, *Ap.J*, **371**, 171.
- Lada, C. J., Gottlieb, C. A., Litvak, M. M., and Lilley, A. E., 1974, *Ap.J*, **194**, 609.
- Lada, C.J. 1985, *Ann. Rev. Astr. Ap.*, **23**, 267.
- Lane, A. P., 1989, in: *ESO Workshop on Low Mass Star Formation and Pre-Main Sequence Object*, ed. Reipurth, B. (ESO, Garching), P. 331.
- Lane, A. P., and Bally, J., 1986, *Ap.J*, **310**, 820.
- Langer, W. D., and Penzias, 1990, *A&A*, **357**, 477.
- Levreault, R. M., 1988, *Ap.J*, **330**, 897.
- Lizano, S., Heiles, C., Rodriguez, L. F., Koo, B. C., Shu, F. H., Hasegawa, T., Hayashi, S. S., and Mirabel, I. F., 1988, *Ap.J*, **328**, 763.
- Maddalena, R. J., Morris, M., Moscowitz, J., and Thaddeus, P., 1986, *Ap.J*, **303**, 375.
- Margulis, M., and Snell, R. L., 1989, *Ap.J*, **343**, 779.
- Masson, C. R., and Chernin, L. M., 1992, *Ap.J*, **387**, L47.
- Masson, C. R., and Chernin, L. M., 1993, *Ap.J*, **414**, 230.
- Matthews, N., and Little, L. T., 1983, *M.N.R.A.S.*, **205**, 123.
- Matthews, N. E., 1993, in: *The James Clerk Maxwell Telescope: A Guide for the Prospective User*.
- Meyers-Rice, and Lada, C. J., 1991, *Ap.J*, **368**, 445.
- Mitchell, G. F., and Hasegawa, T. I., 1991, *Ap.J*, **371**, L33.
- Mitchell, G. F., Hasegawa, T. I., and Schella, J., 1992, *Ap.J*, **386**, 604.
- Moriarty-Schieven, G. H., and Snell, R. L., 1988, *Ap.J*, **332**, 364.

- Moriarity-Schieven, G. H., Snell, R. L., and Hughes, V. A., 1989, *Ap.J.*, **347**, 358.
- Mozurkerewich, D., Schwartz, P. R., and Smith, H. A. 1986, *Ap.J.*, **311**, 371.
- Mundt, R., Witt, A.N., 1983, *Ap.J.*, **270**, L59.
- Mundt, R., Buhrke, T., Fried, J. W., Neckel, T., Sarcander, M., and Stocke, J., 1984, *A&A*, **140**, 17.
- Mundt, R., Brugel, E. W., and Buhrke, T., 1987, *Ap.J.*, **319**, 275.
- Mundt, R. 1988, in : *Formation and Evolution of Low Mass Stars*. A.Dupree and M.T.V.T. Lago (eds.), P257.
- Mundt, R., Ray, T. P., and Raga, A. C., 1991, *A&A*, **252**, 740.
- Parker, N. D., Padman, R., and Scott, P. F. 1991, *M.N.R.A.S.*, **252**, 442.
- Pudritz, R. E., Pelletier, G., and Gomez de Castro, A. I., 1991, in: *The Physics of Star Formation and Early Stellar Evolution*. Lada, C. J., Kylafis, N. D. (eds.), Kluwer, Dordrecht. P. 539.
- Raga, A., 1991, *A.J.*, **101**, 1472.
- Raga, A., and Cabrit, S., 1993, *A&A*, **278**, 267.
- Raga, A., Canto, J., Calvet, N., Rodriguez, L. F., and Torrelles, J. M., 1993, *A&A*, **276**, 539.
- Ray, T. P., Poetzel, R., Solf, J., and Mundt. R., 1990, *Ap.J.*, **357**, L45.
- Reipurth, B., 1989, in : *ESO Workshop on Low Mass Star Formation and Pre-Main Sequence Object*, ed. Reipurth, B. (ESO, Garching), P. 247.
- Richer, J. S., Hills, R.E., and Padman, R., 1992, *M.N.R.A.S.*, **254**, 525.
- Shu, F. H., Adams, F. C., and Lizano, S., 1987, *Ann. Rev. Astr. Ap.*, **25**, 23.
- Shu, F. H., Lizano, S., Ruden, S. P., and Najita, J., 1988, *Ap.J.*, **328**, L19.
- Shu, F. H., Ruden, S. P., Lada, C. J., and Lizano, S., 1991, *Ap.J.*, **370**, L31.
- Snell, R. L., Loren, R. B., and Plambeck, R. L., 1980, *Ap.J.*, **239**, L17.
- Snell, R. L., and Edwards, S., 1981, *Ap.J.*, **251**, 103.
- Snell, R. L., and Edwards, S., 1982, *Ap.J.*, **259**, 668 (SE82).

Snell, R. L., Scoville, N. I., Sanders, D.B., and Erickson, N.R., 1984, *Ap.J.*, **284**, 176.

Solf, J., 1987, *A&A*, **184**, 332.

Strom, K. M., Strom, S. E., and Kinman, T. D., 1974, *Ap.J.*, **191**, L93.

Strom, K. M., Strom, S. E., and Vrba, F. J., 1976, *A.J.*, **81**, 308.

Zealey, W. J., Williams, P. M., Sandell, G., Taylor, R. N. J., and Ray, T. P., 1992, *A&A*,  
**262**, 570.

Zukerman, B., Kuiper, T. B. H., and Kuiper, E.N.R. 1976, *Ap.J.*, **209**, L137.